Inception of Macroscopic Shear Bands During Hot Working of Aluminum Alloys

Aditya Prakash[1,2], Tawqeer Nasir Tak[3], Namit N. Pai[2], Harita Seekala[4], S.V.S. Narayana Murty[5], P. S. Phani[4], Sivasambu Mahesh[6], P. J. Guruprasad[3], Indradev Samajdar[2]

[1] R&D Division,Tata Steel Ltd., Jamshedpur, 831001, Jharkhand, India
[2]Department of Metallurgical Engineering and Materials Science, Indian Institute of Technology Bombay, Mumbai, 400076, India
[3] Department of Aerospace Engineering, Indian Institute of Technology Bombay, Mumbai, 400076, India
[4] International Advanced Research Centre for Powder Metallurgy & New Materials (ARCI), Hyderabad, 500005, India
[5]Vikram Sarabhai Space Centre, Trivandrum, 695 022, India
[6] Department of Aerospace Engineering, Indian Institute of Technology Madras, Chennai, 400076, India

Abstract

Macroscopic shear bands (MSB) may develop during hot working of metallic materials. They are well-understood as a physical manifestation of flow instability, and the processing regimes wherein they form are often charted. However, the microstructural transitions that occur from the onset of flow instability to the MSB inception are not fully understood. In order to elucidate them, several aluminium alloy specimens were subjected to strip testing in a thermomechanical simulator (Gleeble^{TM}) at 298K and 573K. Prominent MSB were observed along the diagonals of the strip volume of only Aluminum-6 weight% Magnesium alloy specimen deformed at 573K. Comparing the experimental grain morphology and crystallographic textures with those from plastic flow models revealed that MSB inception occurred only after ~0.20 homogeneous plane strain deformation. However, classical flow instability was predicted at much smaller strain. This 'delay' was explained experimentally by showing that clusters of neighbouring severely deforming, fragmenting, mostly soft-oriented grains gradually developed due to lattice rotations along the specimen diagonals, and that MSB inception corresponded to the formation of a percolating network of such grains spanning the specimen. Further, clear experimental

evidence revealed that differential dynamic recovery between hard- and soft-oriented grains was essential for MSB formation.

Keywords: Aluminum, Deformation, Microstructure, Macroscopic Shear Band, Modelling.

---

1. Introduction

In the hierarchy of deformation heterogeneities (Dieter and Bacon, 1976; Humphreys and Hatherly, 2012; Verlinden et al., 2007a), macroscopic shear bands (MSB) are the coarsest. MSBs are transgranular in nature, often span the entire specimen, and are the signature of localized material flow driven by material and/or geometrical softening (Semiatin, Lahoti, and Oh, 1983; Semiatin and Jonas, 1984). Adiabatic shear bands may also be regarded as MSBs formed under dynamic conditions. They are thought to arise from material softening accompanying rapid local temperature increase due to plasticity (Dodd and Bai, 2014). However, this view has been be contested recently (Guo et al., 2020, 2019). An alternate mechanism, via continuous dynamic recrystallization or extended recovery (Verlinden et al., 2007b), has been proposed as the cause of associated softening (Magagnosc et al., 2021).

Flow instability, and the formation of MSBs cannot occur without geometrical and/or material softening. This can be inferred from the calculations of Hill (1950) and Green (1951) in the 1950s. Hill (1950) and Green (1951) determined the slip-line fields describing the plastic flow during plane strain indentation of a rigid-perfectly plastic material. They found that the slip lines emerged like a fan from the singularities at the four edges of contact between the dies and the strip. The plastic flow was not localized. Barring small triangular regions contacting the dies that remained rigid, material flowed throughout the specimen. Further, flow localization has been found absent, experimentally, in materials exhibiting the dominance of work hardening (Raabe et al., 2001). However, in materials with significant work softening,

typically realized under hot-working conditions, the flow field has been found to localize within the MSB. MSBs were also observed during different modes of thermomechanical processing, with examples ranging from hot torsion (Semiatin and Lahoti, 1981) to hot forging (Semiatin and Lahoti, 1982) and even plane strain compression in a thermomechanical simulator (Tang et al., 2018). It has been reported (Semiatin and Lahoti, 1982) that MSB inception required considerable additional strain past the point of homogeneous flow instability. This important observation has been pursued further in the present study.

While softening is necessary for MSB formation, the set of microstructural transitions that lead to MSB is not clear. An important milestone in the detailed study of microstructural transitions is due to Korbel et al. (1986) and Korbel and Martin (1986), who studied Aluminum - 4.8 weight% Magnesium. They observed the formation of microbands, or regions of intense localized shear, confined to individual grains. These evolved from a tangle of dislocations after about 20% rolling reduction. With increasing strain, these microbands were able to penetrate grain boundaries, and extend into neighbouring grains. Between 60% and 80% reduction, they reported the formation of MSB extending across the thickness of the specimen. In brief, the dense clusters of microbands transformed into MSB with increasing strain. The microstructural transition from isolated grain-interior microbands to that of the MSB was clearly abrupt. This abrupt transition, however, was not deliberated in depth by Korbel et al. This, arguably, required simultaneous characterization of the microstructure at multiple length scales.

Multiscale characterization techniques, especially various forms of digital image correlation (DIC), have now been extensively developed (Efstathiou et al., 2010). Aydıner and Telemez (2014), for example, established that macroscopic shear bands emerged abruptly, by the explosive propagation of microscopic twins extending several grains in an Mg alloy. On the other hand, Üçel et al. (2019) reported a considerably lower degree of strain localization in

the same alloy under uniaxial tension. However, DIC has not been used to describe initation of MSB in hot worked microstructures.

Technologically, MSB formation limits the range of possible thermomechanical processing operations (Verlinden et al., 2007b), and also affects such diverse areas as metalcutting, ballistics and geology (Semiatin and Jonas, 1984). MSB accommodate large plastic strains and thus introduce deformability or ductility (Needleman et al., 1988). However, the final failure also initiates in the MSB (Deve and Asaro, 1989). MSBs also introduce significant deformation and shear strain strain gradients (Paul et al., 2015). Any post-processing of a deformed material with MSB (for example, strip production from rolled coils) might result in warpage (Mukherjee et al., 2020; Hidveghy et al. 2003). This has been attributed to residual stress accomodation from MSB. In summary, MSB formation in metallic materials is an important aspect of industrial thermomechanical processing. Understanding the mechanisms of MSB formation may enable the development of techniques for their avoidance, or control, and thereby extend the capabilities of metal forming, and other operations.

The present work aims to uncover the microstructural transitions leading up from mesoscale strain localizations to the inception of MSB. To this end, specimens from several aluminum alloys were subjected to plain strain indentation (strip testing) in a thermomechanical simulator (Gleeble™). These tests were conducted at both ambient (298K) and elevated (573K) temperatures, the latter was followed by water quenching. MSB formation was prominently observed in coarse-grained Aluminum - 6 weight% Magnesium (Al-6Mg) alloy deformed at 573K. These conditions fall outside the extensively studied Portevin-LeChatelier regime (Reyne et al., 2020; Xu et al., 2022; Yuzbekova et al., 2017), and outside the superplastic regime (Zha et al., 2021). Nominally identical specimens of Al-6Mg were subjected to progressive plastic deformation and their ex-situ microstructures were extensively

characterized. Comparing these microstructures, and local crystallograophic textures with predictions from a polycrystal plasticity model yielded physical insights into the flow fields. This led to an accurate estimate of the strain for MSB inception, and allowed an examination of the transition from the localized to global shear deformation mode within the MSB.

2. Experimental Procedure

This study used four different aluminum alloys: AA1050, AA2219, Al-3Mg, and Al-6Mg. The chemical compositions are given in table 1. It is to be noted that all these grades were obtained from the Indian Space Research Organization (ISRO) as hot rolled plates. These were then processed by cold rolling, recrystallization, grain coarsening anneals, and finally solution treatment to obtain fully recrystallized solutionized material. It is to be noted that the alloys were processed to have similar average grain sizes (~120 μm) and near-random crystallographic textures (to be discussed latter in the experimental results). Strip tests were conducted using a constant strain rate (0.1 s^{-1}) and a standard (Verlinden et al., 2007b) Gleeble^{TM} 3800 set-up. The top die (with respect to the specimen) represents the stroke side, whereas the bottom portion is indicative of the wedge side (see figure 1a). 'J' type thermocouples were spot welded to the specimen; to provide an accurate measure of the specimen temperature.

Table 1: Chemical composition (in weight% alloying elements) of the alloys (AA1050, AA2219, Al-3Mg and Al-6Mg) used in this study.

	Mn	**Si**	**Cr**	**Cu**	**Fe**	**Mg**	**Al**
AA 1050	0.002	0.088	0.003	0.003	0.1	0.002	99.8
AA 2219	0.30	0.1	-	5.86	0.12	0.016	93.3
Al-3 Mg	0.76	0.094	0.13	0.017	0.16	3.6	95.92
Al-6 Mg	0.66	0.16	0.008	0.011	0.14	6.55	92.4

A few deformed specimen geometries have been shown using optical micrographs in figures 1a and 1b. The sample geometry used is shown in figure 1a. This was based on Loveday et al. (2006) and ASTM E209-18 ("Standard Practice for Compression Tests of Metallic Materials at Elevated Temperatures with Conventional or Rapid Heating Rates and Strain Rates", 2018) standards. Further, post deformation samples were water-jet cooled (~200K/s cooling rate, as measured at the specimen surface). All 'strip' testing measurements were repeated three times, to ensure reproducibility in the aforementioned data. Appropriate specimen cross-sections, mid-width and mid-thickness sections of the 'strip' tested (Gleeble™) specimens were then used for detailed microstructural characterizations.

The long transverse (LT) plane, containing the rolling (RD) and normal (ND) directions, was prepared by a combination of traditional metallography and electropolishing. Electropolishing was performed using Struers™ Lectropol-5 equipment. An electrolyte of methanol and perchloric, 80:20 ratio, was used at 273K and 13 volts dc. Electron backscattered diffraction (EBSD) was performed on an EDAX-OIM™ system. This system was integrated with a FEI™ Quanta-3d field emission gun (FEG) scanning electron microscope (SEM). The step size, beam and video conditions were identical between the scans. Bulk residual strains were measured with multiple {hkl} GIXRD (grazing incident X-ray diffraction) (Prakash et al., 2022b; Reimers and Dupke, 1995; Thool et al., 2020; Vanhoutte and L, 1999; Withers and Bhadeshia, 2001) in a PANalytical™ Empyrean system. This study also used transmission electron microscopy (TEM). For these, the samples were prepared (with a similar electropolishing protocol, as mentioned earlier) in a Struers™ Tenupol-5 twin jet electropolisher. The TEM characterization was conducted in a Thermo-Fisher™ Themis-300 microscope.

Nanoindentation tests were performed using a commercially available nanoindenter, iMicro™ from Nanomechanics Inc.™ (now KLA corporation), Oak Ridge, USA. A diamond

Berkovich indenter tip (E = 1141 GPa; ν = 0.07) was used for all the tests. Two different test methodologies were used to test the samples, a constant strain rate indentation test with continuous stiffness measurement (CSM) and high-speed mapping using the NanoBlitz 3D module. The CSM-based tests were performed as per the guidelines specified elsewhere (Sudharshan Phani et al., 2021) to a maximum load of 45 mN, wi th an oscillation frequency of 1 kHz and a dynamic load to mean load ratio of 0.2. The high-speed mapping was typically carried out over a 150 μm x 20 μm area at a 1 mN load and an indentation spacing of 1 μm. These parameters were chosen based on a recent study (Sudharshan Phani and Oliver, 2019) to ensure the minimal influence of neighboring indents. A few additional maps with similar spacing but different scan areas were also performed.

3. Results

3.1. Experimental Results

Figure 1a shows the physical appearance of a deformed specimen and the formation of severe flow localization on the LT plane within macroscopic shear bands or MSB. It is to be noted that the final fracture also took place in the MSB (see figure 1a). The stress-strain responses from 'strip' tests are collated in figure 1b (for Al-6Mg) and figure 1c (for different aluminum alloys). The anisotropy in crystallographic texture can be represented as texture index or $\int f(g)^2\, dg$ (Vadavadagi et al., 2016; Yerra et al., 2005). It is to be noted that a texture index of ~1 represents a truely randomized texture. As shown in supplementary material S-3, all our aluminum alloys had nearly randomized starting (before strip testing) textures, with texture indices between 1.3-1.5.

As shown in figure 1b, Al-6Mg showed limited ductility, and no softening or optically-visible MSB formation, during room temperature (298K) deformation. In contrast, at 573K

the same material showed much higher ductility and clear softening. It is apparent from figure 1b that high-temperature deformation in Al-6Mg, where clear softening accompanied stress-strain response, was accompanied by visible MSB formation. Figure 1, in a sense, justifies Needleman's statement (Needleman et al., 1988) on macroscopic plastic instabilities – both as a precursor to fracture and a mechanism behind large-scale plastic deformation and ductility. As our Gleeble^{TM} set-up (figure 1a) was identical in all cases, enabling similar plastic flow or velocity fields, the explicit softening (figure 1b-c) and the material properties appeared essential for the appearance or formation of MSB. Though past research (Backofen, 1973; Dillamore et al., 1979; Estrin and Kubin, 1986; Harren et al., 1988b; Jia et al., 2012; Mathur and Backofen, 1973; Semiatin, S. L., Lahoti, G. D., & Oh, 1983) also attributed MSB formation to negative strain hardening, figure 1c provides a nice summary of this attribute. High temperature and high Mg content and the associated softening were clearly essential. This study was then extended to the microstructural attributes of progressive (imposed strains of 0.12, 0.28 and 0.69) MSB formation in the Al-6Mg.

Figure 2a shows the progressive microstructure evolution associated with the MSB formation in Al-6Mg at 573K. It is important to note that three different, but nominally identical Al-6Mg samples, are loaded to true strains of 0.12, 0.28 and 0.69, as shown in figure 2a. The initial microstructures of all three specimens are not shown here for brevity. The starting microstructure was strain-free or misorientation free. The latter was quantified using kernel average misorientation, or KAM values. KAM represented misorientation of each measurement point with respect to its immediate six neighbors in a hexagonal grid, provided any such misorientation did not exceed 5°. It is to be noted that KAM scales (Fu et al., 2022; Harte et al., 2020; Pai et al., 2022; Prakash et al., 2022a) with geometrically necessary dislocation (GND) density. Further, KAM is less sensitive to step size than GND density estimates. In our study, we have used a step size of 0.6 μm for large area (example, figure 2a) and 0.1 μm for high

resolution (example, figure 2c). These (especially, significant differences in EBSD step size) necessitated use of KAM over GND in our analysis.

The optical appearance of the MSB (figure 1), was clearly reflected in the KAM localization, see figure 2a. Progressive KAM localization with increasing strain only occurred in Al-6Mg at 573K. The optical micrographs are shown in figure S-1.1. The figure clearly shows that MSB formation was most severe in Al-6Mg, followed by Al-3Mg. This was, however, absent in AA1050 and AA2219. In these latter specimens, it either never initiated, or initiated and stopped at a much smaller strain.

Direct experimental observations on MSB formation were also collated. As presented in figure 2b, and indicated qualitatively earlier in figure 2a, the signatures of plastic deformation were largely restricted within the MSB. For example, the KAM values, the grain elongation (or grain aspect ratio) and the presence of fine grains (grains smaller than $10\,\mu m$, clearly originating from the plastic deformation) were localized inside the MSB. Plastic deformation (at least in terms of relative KAM values, and even grain aspect ratio) appeared to extend beyond the MSB only at $\varepsilon = 0.69$, which was very close to the fracture strain. Another interesting aspect of the MSB microstructure was brought out through higher resolution imaging with EBSD (with smaller step size and better spatial resolution) and TEM, see figure 2c. Inside the MSB, the dislocation substructures appeared more recovered and associated with relatively well-defined dislocation boundaries. Korbel et al. (1986) associated the formation of strain localization with dynamic recovery as well. The observations in figure 2c are thus not unexpected. Later, more definitive (and quantitative) evidence on this, especially differential dynamic recovery, would be presented.

This study also used nano-indentation measurements, and corresponding hardness maps, to investigate MSB formation. Figure 3a shows optical images and a corresponding

hardness map of undeformed Al-6Mg. Nano-indentations could differentiate between the hardness of differently oriented grains and resolve coarse 2nd phases. Further, nanoindentations maps (figure 3b) qualitatively distinguish between the inside and outside of MSB. This appeared in terms of the hardness differential and more so from the dislocation pop-in size (see figure 3c). The latter, expanded elsewhere (Li et al., 2011; Sudharshan Phani and Oliver, 2020; Wang and Ngan, 2004), indicates the availability of mobile dislocations during nano-indentation tests. For the estimation of pop-in size, from nano-indentation data, the reader may refer to supplementary data S-2.

It is to be noted that in addition to the defect structure (or presence of mobile dislocations), the pop-in size depends on several factors (including pop-in load). This would prevent a unique quantitative relationship between mobile dislocation density and pop-in size, but a semi-quantitative comparison appears feasible. Our measurements of the pop-in size (figure 3c) thus represent dislocations that were not in low energy or stable configuration and were made 'mobile' during the nano-indentation measurements.

Dislocation pop-in size (see figure 3c) can thus be taken as a measure of dynamic recovery. The marginal hardness difference (figure 3b and 3c) but more significant pop-in size difference (figure 3c) clearly differentiated between inside and outside of the MSB at $\varepsilon \sim 0.28$. However, close to the failure strain ($\varepsilon \sim 0.69$), this distinction was largely eliminated. In other words, the interior of the MSB showed higher dynamic recovery both microstructurally (figure 2c) and from indirect but semi-quanititative measures of pop-in size (figure 3c). It is to be noted that a strong influence of dynamic recovery on MSB formation is quite expected (McQueen and Jonas, 1975). Later in section 4.3, measurements of dynamic recovery have been extended to the so-called hard and soft crystallographic orientations, and the role of differential dynamic recovery on the MSB formation will be proposed.

It can be determined from figure 1b that $\frac{\partial^2\sigma}{\partial\varepsilon^2} = 0$ at $\varepsilon \approx 0.24$, in Al-6Mg deformed at 573K. Thus, there is an inflection point in the stress-strain curve for Al-6Mg. In the literature, inflection points have been identified as strong signatures of the onset of dynamic recrystallization (Poliak and Jonas, 1996, 2003). However, no microstructural signature of dynamic recrystallisation has been observed presently. This is consistent with a finding of Mostafaei and Kazeminezhad (2012) in the same material. They concluded that the inflection point in the stress-strain curve was fictitiously caused by die friction and adiabatic heating. On correcting for these effects, they showed that the inflection point vanished.

The MSB formation was visible in optical imaging (figure 1) and more so in EBSD image quality (IQ) maps, see figure 4a. We have taken estimates of KAM and residual strain, along the rolling direction or RD, and at different locations of the strip tested specimens (see figure 4b). The residual strains were measured with multiple {hkl} GIXRD by using an X-ray lens (Lodh, 2018; Lodh et al., 2019; Thool et al., 2020). It is to be noted (Lodh et al., 2019, 2017; Prakash et al., 2021) that the residual strain values are expected to be a function of both GND density and the dislocation configuration. The KAM, on the other hand, scales with GND density. Figures 4b thus shows quantitative evidence for increased localized plastic deformation associated with the MSB formation. In particular, the region of the MSB contained higher GND density and residual strain. The microstructural transitions leading to MSB formation have been sought through plasticity modeling.

3.2 Plasticity Modeling

Polycrystal plasticity simulations, using a binary-tree-based model (Mahesh, 2010), were conducted to predict the texture evolution at the different locations in the deformed specimen. In our simulations, the grains were assumed to be rigid when the stress-state was within the yield surface of the stress space, i.e., elastic deformation was neglected. Further,

plasticity on the yield surface was assumed to be rate-independent. The critical resolved shear stresses of the slip systems, τ, were set equal to unity. They were not evolved during the simulated deformation. The simulations covered an aggregate of 256 grains, whose orientations and volumes were drawn randomly from EBSD measurements of the initial texture (Singh et al., 2017). Lattice rotations in the grains were tracked for two qualitatively different flow fields, as detailed below.

3.2.1 Flow Fields

The directions RD, TD, and ND are recalled from figure 1. Let these directions be associated with the sample-fixed coordinate axes, x_1, x_2, and x_3, respectively. The unit vector along the x_i coordinate axis is denoted $\vec{e}_i$. Let the origin O be located at the centre of the specimen, as shown in figure 5a. Because of symmetry, there will be no flow across the x_1-x_2 and x_1-x_3 planes. Thus, it suffices to restrict attention to the octant $x_1 \geq 0,\ x_2 \geq 0, x_3 \geq 0$.

Let the dies be of width $2a$, and let the initial thickness of the specimen be $2H$. Presently, $2a = 5$mm, and $2H = 10$mm (figure 1). Let the dies move toward the origin with constant speed V. Consider an instant during the deformation, when the thickness of the specimen has decreased to $2h < 2H$. If time were reckoned from the instant at which indentation started, this instant would correspond to time $t = (H - h)/V$.

Consider first the condition of homogeneous plane strain compression (PSC). Let $v_i(x_j)$ denote the i-th component of the material point velocity at position x_j. At $t = (H - h)/V$, the velocity gradient corresponding to plane strain compression is given by

$$L_{ij}^{PSC} = \frac{\partial v_i}{\partial x_j} = \frac{V}{h}\begin{pmatrix} 1 & 0 & 0 \\ 0 & 0 & 0 \\ 0 & 0 & -1 \end{pmatrix}. \text{----------}(1)$$

The components of L_{ij}^{PSC} increase in magnitude as $h \downarrow 0$, i.e., as the dies approach each other.

Next, consider the case of localized shearing along the diagonals between the dies, wherein the material points away from the diagonals translate rigidly, as shown in figure 5b.

The following is a quantitative version of the block shear model of Semiatin and Lahoti, 1982. Let θ be the inclination of a slip line positioned along the specimen diagonal to the x_1 axis, as shown in figure 5c. Then, $\tan\theta = h/a$. For volume conservation, the normal velocity of the material point as it traverses the diagonal slip-line must be constant (Johnson et al., 1982). This implies that the speed of the material point, as it emerges from the slip line must be $V/\tan\theta = Va/h$, as shown in figure 5c.

Material points with finite normal speed traverse the diagonal slip-lines of infinitesimal thickness in infinitesimal time. This makes the velocity gradient within the slip-lines undefined. To obtain a finite velocity gradient history for material points passing through the slip-lines, slip is assumed to occur in a zone of thickness δ, as shown in figure 5d. The velocity field in this zone, consistent with the inlet and outlet velocities, is taken to be

$$\vec{v} = -V\overrightarrow{e_3} + \frac{\vec{x}.\vec{n}}{\delta}\left(\frac{Va}{h}\overrightarrow{e_1} - (-V\overrightarrow{e_3})\right), \text{----------(2)}$$

where $\vec{n} = \sin\theta\,\overrightarrow{e_1} - \cos\theta\,\overrightarrow{e_3}$. It is noticed that $\vec{x}.\vec{n} = 0$, at the inlet to the δ −zone, and $\vec{x}.\vec{n} = \delta$, at the outlet, as shown in figure 5d.

Differentiating the velocity field with respect to the spatial coordinate x yields the velocity gradient within the MSB:

$$L_{ij}^{MSB} = \frac{\partial v_i}{\partial x_j} = \frac{V}{\delta}\begin{pmatrix} \cos\theta & 0 & -\cos\theta\cot\theta \\ 0 & 0 & 0 \\ \sin\theta & 0 & -\cos\theta \end{pmatrix} = \frac{V}{\delta\sqrt{a^2+h^2}}\begin{pmatrix} a & 0 & -\frac{a^2}{h} \\ 0 & 0 & 0 \\ h & 0 & -a \end{pmatrix} \text{----------(3)}$$

The material point spends a finite time, Δt_δ, within the δ-zone: $\Delta t_\delta = \delta/(V\cos\theta) = (\delta/V)\sqrt{a^2+h^2}/a$. It is seen that although the regularised velocity gradient L_{ij}^{MSB} and time Δt_δ depend on the slip zone width δ, and die speed V, the product $L\Delta t_\delta$ does not. The deformation imparted to the material point is thus independent of both the regularization parameter δ, and the die speed V. Furthermore, as the model material is rate-independent, the values assigned to δ, and V are unimportant. Presently, therefore, they are set to unity.

3.2.2. Material Point Tracking

It is seen in the previous section that for block shear flow, the velocity gradient experienced by the material point depends on the instant at which it passes through the diagonal slip-lines. This instant can be specified in terms of either h or θ. In microstructural analyses of a deformed specimen, it is interesting to determine h and/or θ for each point $(x_1, 0, x_3)$ in the LT-section of the specimen. To this end, suppose the specimen was extracted for microstructural analysis when the die gap was $2h_m$.

Suppose the material located at $(x_1, 0, x_3)$ passed through the slip-line at a time T before test interruption and specimen extraction. In this time, it would have translated by

$$\int_0^T \frac{Va}{H-Vt} dt = -a \ln\left(1 - \frac{VT}{H}\right) \text{ ----------(4)}$$

along the x_1 direction. This is obtained by integrating the outflow velocity at the slip line over time. Thus, the spatial position of the point on the slip-line whereat it crosses the slip line is $(x_1 + a \ln[1 - VT/H], 0, x_3)$. But the die-gap at time T before specimen extraction would be $2h_m + VT$. These considerations lead to the following transcendental equation for the unknown T

$$\frac{x_3}{x_1 + a \ln(1 - VT/H)} = \frac{h_m + VT}{a}. \text{ ----------(5)}$$

This equation can be solved numerically using the method of successive bisection. If this equation has a solution for given $(x_1, 0, x_3)$, it indicates passage of the material point through the slip-line during material indentation. The absence of a solution indicates the material point has never undergone localized deformation. Further, the half die-gap corresponding to the instant at which the material point passed through the slip line is given by $h_m + VT$, so that $\theta = \tan^{-1} \frac{h_m + VT}{a}$.

3.3. Results from Plasticity Modelling

The material point tracking method above was applied to the Al-6Mg specimen deformed at 573K to $\varepsilon = 0.69$. A uniform 100×100 point grid in the $x_2 = 0$ plane, extending from $0 \leq x_1 \leq a$, and $0 \leq x_3 \leq h_m$ was setup. At each point of the grid, $\theta(x_1, 0, x_3)$ was determined, and the contour lines of θ were drawn. Figures 6a and 6b show these contour lines superposed on the EBSD-IQ maps of the deformed specimen. The innermost and outermost contour lines, with $\theta \approx 45°$ and $\theta \approx 62°$, corresponded to material points that deformed latest and earliest during testing, respectively. The contours of figure 6a were plotted assuming that MSB initiates right from the beginning, $\varepsilon = 0$, while those of figure 6b assumed MSB initiation only after $\varepsilon = 0.20$. In figure 6a, some rounded, undeformed grains are observed in the area near the earliest, or the outermost contours. This indicated that the assumption of MSB initiation from the beginning of indentation was incorrect. On the contrary, all the grains in the area enclosed by the contours are elongated in figure 6b, indicating that the MSB deformation initiated only after $\epsilon \approx 0.20$.

The transition from the homogeneous PSC to localized MSB mode was further confirmed by experimental measurements and numerical simulations of crystallographic textures outside the localized regions of the deformed specimen, labelled 'outer region' in figure 4a. These regions were cropped out, and the representative orientation distribution function $f(\phi_1, \phi, \phi_2)$ was calculated using the TSL-OIM^{TM} software.

The grains in the outer region are assumed not to deform once the MSB deformation mode sets in, following Semiatin and Lahoti (1982). If so, the texture evolution of the grains in this region carries the signature only of the homogeneous PSC mode. To determine the extent of the PSC mode, forty texture simulations assuming the homogeneous PSC mode were run for $\varepsilon \in \{10\%, 11\%, \ldots, 50\%\}$. The ODF of the predicted final textures is calculated again, using the TSL-OIM software. For estimating arithmetic differences between experimental and

simulated textures, we have used Texture Difference Index (ID_N) (Raveendra et al., 2011). The reader may refer Appendix B for the formulation. Further, our best texture simulation provided ID_N values between 0.82-0.99. These very low values (Raveendra et al., 2011) provide quantitative confirmation on the accuracy of our simulations, and estimations of the strain mode.

The variation of the texture difference indices with ε is shown in figure 6c. The best agreement between the experimental and simulated textures, indicated by the smallest texture difference index, occured if the simulations imposed homogeneous deformation following L_{ij}^{PSC} up until $\varepsilon = 0.19$, followed by L_{ij}^{MSB}, until the end of the deformation. This transitional value is remarkably close to the transitional value of $\varepsilon = 0.20$ obtained using material point tracking. With the transitional point from homogeneous to localized flow in hand, texture predictions were made for the various regions of the specimen. Figure 6d compares these predictions with experimentally measured textures. Model grains were assumed to obey homogeneous PSC flow at the centre of the specimen, where the MSB arms intersect (first row of figure 6c). Outside the MSB, grains were assumed to deform following the homogeneous PSC mode up to $\varepsilon = 0.20$, and remain undeformed thereafter. Within the arms of the MSB, grains are assumed to deform following the homogeneous PSC mode up to $\varepsilon = 0.2$, followed by the inhomogeneous MSB mode. In all the three regions, the predicted textures agreed well with the experimentally measured ones. This validated the model flow fields and their operative regimes a function of ε.

4. Discussion: Combining Microstructure and Plasticity modeling

MSB formation has been reported in both precipitation-hardenable (Chang and Asaro, 1981; Harren et al., 1988a; Wagner et al., 1995) and strain-hardenable (Korbel et al., 1986; Korbel and Martin, 1986) aluminium alloys. Hence, we have considered both alloys, bound by

a common thread of application in ISRO's (Indian Space Research Organization) launch vehicles. It is shown in this section that MSB formation is determined by its mechanism, and not by the nature of the aluminum alloy.

4.1. Flow instability

According to the classical Considière (Considère, 1885) criterion, adapted to the present case of compression between dies of fixed area, flow instability is predicted when the hardening rate, $\partial\sigma/\partial\varepsilon$, becomes negative. In terms of the non-dimensional hardening rate, γ, the condition for instability is:

$$\gamma = \frac{1}{\sigma}\frac{\partial\sigma}{\partial\varepsilon} \leq 0. \text{ ----------(6)}$$

Hart (1967) and Jonas et al. (1976) studied strain localisation during uniaxial tension and compression. Jonas et al. (1976) observed that equation (6) represented the condition for the *onset* of flow localisation. For flow localisation to result in failure, they noted that the *rate* of strain localisation must be quantitatively large. For the present case of compression between dies of fixed area, Semiatin and Lahoti (1982) showed that the non-dimensional rate of strain localization, $\alpha = \frac{1}{\dot{\varepsilon}}\frac{\partial\dot{\varepsilon}}{\partial\varepsilon}$, is related to the non-dimensional hardening, γ of equation (6) through the simple expression:

$$\alpha = \frac{1}{\dot{\varepsilon}}\frac{\partial\dot{\varepsilon}}{\partial\varepsilon} = \frac{-\gamma}{\mathrm{m}}, \text{ ----------(7)}$$

where, $\mathrm{m} = \partial \ln\sigma/\partial \ln\dot{\varepsilon}$, denotes the strain-rate sensitivity of the material. Following a suggestion of Jonas et al. (1976), Semiatin and Lahoti (1982) expected MSBs to be well-developed when $\alpha \geq 5$. This criterion is also adopted presently.

Figure 7a plots the variation of γ and α with deformation in the Al-6Mg specimen deformed at 573K. This figure was deduced from the stress-strain behavior shown in figure 1b. For calculating α, it was assumed that $m = 0.14$, as measured by Romhanji et al. (2002). The Considière condition, equation (6), predicted the onset of flow instability at $\varepsilon_{PSC} \approx 0.05$, while

Semiatin and Lahoti's criterion, equation (7), indicated failure at $\varepsilon \approx 0.12$. Both predictions, however, preceded the MSB inception strain, $\varepsilon \approx 0.20$, obtained experimentally in section 3.3. This observation is consistent with Semiatin and Lahoti's (1982) observation that during the hot forging of a titanium alloy, the predicted strain of failure consistently preceded that of actual MSB inception.

In order to explain this discrepancy, it is presently proposed that although the necessary *dynamic* mechanical condition for instability has been satisfied, flow localization in the form a physical MSB extending across the specimen would not incept until the *kinetic* condition of strain percolation across the specimen has been completed. In other words, the dynamic mechanical instability condition is only a necessary, but not a sufficient condition for MSB formation. To establish this argument further, and thereby to define the origin of MSB formation, experimental data and data interpretation on strain percolation and differential dynamic recovery are presented in the following sections.

4.2. Strain Percolation

The notion of the percolating strain path was introduced by Raabe et al. (2001). They performed quasistatic channel die compression on a coarse aggregate of columnar aluminum grains, and modeled the same using finite element analysis. They observed strain concentrations along the diagonals of gauge section. More significantly, even within the diagonal regions, strain concentrations were localized among the soft grains, whose lattice orientations were more favorable for slip. Since these tests were performed at room temperature, at which aluminum has a hardening response, the diagonal strain concentrations did not evolve into MSB.

Following Raabe et al. (2001), the present Al-6Mg grains were conceptually regarded as being separated into soft and hard orientations, with the former accommodating most of the imposed deformation. Figure 7b shows a high resolution (HR-) EBSD scan performed at the

MSB interface. It showed significant grain fragmentation of soft-oriented (average Schmid factor = 0.45) grains. The low angle grain boundaries that demarcated the fragments are indicated by blue lines. The high misorientation signatures in the KAM map within the soft grains also indicate significant orientation gradients. Such grain fragmentation was clearly absent in the hard-oriented (low Schmid factor) grains.

It was sought to understand the distribution of fragmented grains in the specimen, in figure 7c. To this end, the centroids of all the grains identified by the EBSD scan were indicated as blue dots. If a pair of neighboring grains were both smaller than $300\ \mu m^2$ in area (less than 10% of the average grain area), they were regarded as grain fragments, and their centroids were joined by a red line. It was seen in figure 7c that in Al-6Mg deformed at 573K, isolated small clusters of fragmented grains at $\varepsilon \approx 0.12$ developed into a specimen-spanning percolating network at $\varepsilon \approx 0.28$, and that the network became more extensive and denser at $\varepsilon \approx 0.69$. The percolating network developed within the MSB region recognised visually in figure 1. However, the percolating network did not span all the grains within the MSB region. A number of non-fragmented grains were seen as islands within the network at $\varepsilon = 0.28$, and $\varepsilon = 0.69$ in figure 7c. The fraction of such non-fragmented grains was seen to decrease with increasing strain, ε. At $\varepsilon \approx 0.12$, $\varepsilon \approx 0.28$, and $\varepsilon \approx 0.69$, the number fraction of unfragmented grains in figure 7c was 91%, 28%, and 16%, respectively. In further consonance with figure 1, the percolating network developed only in Al-6Mg deformed at 573K. It neither developed in the other tested alloys at any temperature, nor in Al-6Mg deformed at room temperature. These observations showed that the microstructural network of neighbouring fragmenting grains and the MSB were closely connected.

Figure 7d shows the cumulative distribution of the Schmid factors of the fragmented grains identified at the three strain levels shown in figure 7c. The distribution of Schmid factors is nearly independent of the strain level, ε. Furthermore, the fragmented grains are

predominantly soft-oriented: Only about 20% of the fragmented grains have Schmid factor smaller than 0.42. The remaining 80% of the fragmented grains are soft-oriented.

To further elucidate the network of fragmenting grains, EBSD scans were obtained for the $\varepsilon = 0$ and $\varepsilon = 0.69$ specimens at the MSB interface, as shown in figure 8a. Before deformation, the scanned area had a majority of intermediate- or soft-oriented grains. Soft grains, coloured red, however, did not form a continuous network. This clearly showed that in the initial microstructure, a network of soft grains was not already present. Thus, the network of figure 7c could not have formed by the fragmentation of pre-existing soft grains only.

Post deformation, bands of fragmented soft grains were clearly noticeable within the MSB. A few elongated stripes of hard orientations are also visible within the MSB. Figure 8b shows HR-EBSD images, and the distribution of KAM obtained from scans taken within the MSB after deformation to $\varepsilon = 0.69$. It is clearly seen that soft grains, coloured red, developed extensive microshear bands (Korbel, 1990), which were responsible for their fragmentation. On the contrary, intermediate, and hard oriented grains did not develop microshear bands, and remained unfragmented. Figures 8c and 8d present these observations quantitatively. They showed that both the KAM and the fraction of low angle grain boundaries (LAGB), with misorientations in the range of $5^{\circ} - 15^{\circ}$, positively correlated with the Schmid factor of the grains. In fact, the LAGB fraction is seen to grow rapidly over the Schmid factor range from $0.42 - 0.50$, i.e., amongst the soft grains.

Figures 7 and 8 proved that while the majority of the percolating network of fragmented grains have soft orientations, a small fraction of the fragmented grains were also intermediate, or hard-oriented. They also proved that the MSB region was not comprised exclusively of soft-oriented fragmented grains; it also contained some non-fragmented hard-oriented grains. The number fraction of hard grains, however, decreased with increasing strain. These exceptions notwithstanding, intensely deforming highly fragmented grains were predominantly soft

oriented (high Schmid factors), and lightly deforming unfragmented grains were hard oriented (low Schmid factors).

The flow field transition from L_{ij}^{PSC} to L_{ij}^{MSB} at $\varepsilon \approx 0.20$ was used to characterize MSB inception mechanically in section 3.2.1. In figure 7c, at $\varepsilon = 0.12$, there was no specimen-spanning (percolating) network. However, a percolating network of intensely deformed grains was observed at $\varepsilon = 0.28$, and $\varepsilon = 0.69$. Although the latter network did not fill the MSB region, it provided a continuous path comprised of highly deformable, mostly soft oriented grains that traversed the specimen in the normal direction (ND). The concentration of the network in the MSB region, and its transition from isolated clusters at $\varepsilon = 0.12$, to a percolating network at $\varepsilon = 0.28$ strongly suggested that the percolation of the network of fragmented grains was the microstructural event marking MSB inception.This implied that the delay in MSB inception past the strain of flow instability, noted in section 4.1, was because of the absence of a specimen-spanning continuous path comprised of highly deformable grains.

Since Al-6Mg at 573 K has a softening response (figure 1), it is expected that soft grains will become softer still with accumulating strain. The underlying mechanism will be experimentally established in the following section. The mechanism for the formation of a percolating network of mostly soft grains post deformation, despite the absence of a percolating network of soft grains in the initial microstructure, will be addressed in section 4.4.

4.3. Differential Dynamic Recovery

Customarily, the formation of MSB has been attributed to definitive softening in stress-strain response (Semiatin, S. L., Lahoti, G. D., & Oh, 1983; Semiatin and Jonas, 1984) and dynamic recovery (McQueen and Jonas, 1975). In our study, the softening in the stress-strain response (figure 1c) coincided with microstructural attributes of dynamic recovery. The latter appeared in the clear differences in deformed microstructures (figure 2c) and in the indirect measure of average pop-in size (figure 3c). It is thus clear that dynamic recovery, in general,

was essential for MSB formation. The strain percolation, on the other hand, indicated the possibility of differential dynamic recovery. In other words, it has been proposed, in this study, that the soft grains recovered more than the hard grains and thus accommodated more deformation and grain fragmentation. This hypothesis would be difficult to validate from hardness and/or misorientations, as the respective differentials were not significant. Further, any observed difference in substructures would be qualitative, requiring more quantitative bulk measurements. We have hence attempted the use X-ray resolution function(XResF) defined as:

$$XResF = \frac{I_{min} - I_b}{I_{k_{\alpha_1}} - I_b}, \text{----------} (8)$$

where, I_{min} is the minimum intensity of the $k_{\alpha_1}/k_{\alpha_2}$ doublet, $I_{k_{\alpha_1}}$ is the maximum peak intensity of the k_{α_1} peak and I_b is the background intensity. XResF, in particular, would represent the separation of $K_{\alpha 1}$ and $K_{\alpha 2}$ of a corresponding XRD peak, and thus represents for dislocation substructure's ability to impart X-ray scattering (Khatirkar et al., 2012; Mukunthan and Hawbolt, 1996), and indirectly represents the energy associated with the corresponding dislocation substructure. Such measurements were used to quantify overall recovery and even recovery in a class of crystallographic orientations (Khatirkar et al., 2012; Mukunthan and Hawbolt, 1996).

This study extended XResF measurements for individual crystallographic orientation(s). From our earlier single-crystal micro-Laue residual strain measurements (Lodh, 2018), we knew how to track a specific crystallographic orientation in an Eulerian cradle. Further, high-resolution Lynxeye™ linear detector enabled accurate measurement of $K_{\alpha 1}$ and $K_{\alpha 2}$ sepeartions (see figure 8a) for specific orientation(s). In order to bring out the orientation dependent differential dynamic recovery, we have conducted our XResF measurements on two extreme (in terms of Schmid factor) crystallographic orientations. These were the hard (Copper {112} <111>, Schmid factor 0.31) and soft (Brass {011} <211>, Schmid factor 0.42)

orientations, respectively. The reader may refer to Prakash et al. (2022) for a brief description of the Schmid factor calculations.

In the fully recrystallized material, both hard and soft orientations showed excellent peak separation and similar, albeit low, XResF values (~0.22). Deformation, as expected, smudged the peak separation and increased the XResF to ~0.99. Further, the numerical values of XResF appeared significantly different between hard copper (0.81) and soft brass (0.48) in Al-6Mg deformed at 573K. Such a striking difference was not present in other alloys (example AA1050) and/or room temperature deformation. These bulk XResF measurements (figure 8a) were further extended with EBSD imaging (of high spatial resolution – see figure 8b) and TEM observations (figure 8c). Figure 8b, for example, showed deformation heterogeneities in deformed Copper, but not Brass grain(s). Further, Brass appeared to show evidence of lower energy dislocation substructure (figure 8c).

In other words, our bulk and local orientation dependent recovery estimates clearly revealed (figure 8) differential dynamic recovery in favour of soft (example - Brass {011}<211>) orientations only in Al-6Mg 'strip tested' at 573K. This also coincided with the appearance and propagation of MSB. It thus appeared that MSB formation plus propagation originated from differential dynamic recovery of crystallographically softer grains or orientations. This enabled percolation of fragmented soft grains, ultimately responsible for the transition in velocity gradients (for homogeneous to localized shear) and formation of macroscopic shear banding.

Prakash et al. (2022) used discrete dislocation dynamics, with additional inputs from molecular dynamics, to bring out the origin of orientation dependent dislocation substructure formation in aluminum alloys. This did depend on both solute content and working temperature. It was perceived that the solute, or Mg-atoms, provide static obstacles and alter the dislocation drag coefficient and probability of cross-slip. In this approach, dislocations moving on a slip plane meet other dislocations at slip plane intersections. This might, based on

the nature of pinning, lead to junction formation. Such junctions, in turn, would act as dynamic obstacles or sources. It was shown numerically that the so-called dynamic obstacles control slip band formation Prakash et al. (2022) as well as orientation dependent substructure creation. In other words, generation of dynamic obstacles is a key factor in dislocation dynamics, which depends on solute plus working temperature. This is also expected to be the governing mechanism behind the differential dynamic recovery reported (figure 8a) in the present study.

4.4 Role of Lattice Rotation

It is still not clear how a percolating network comprised predominantly of soft oriented fragmenting grains develops, even though a percolating network of soft grains is absent in the initial microstructure, as shown in section 4.2. To uncover this final link underlying the kinetics of MSB formation, a binary tree based model polycrystal (section 3.2) comprised of equal numbers of near-brass and near-copper oriented grains, each of the same volume, was considered. The near-brass and near-copper oriented grains were randomly misoriented within 15° of the ideal brass and ideal copper orientations. In the model, each near-brass grain was paired with a near-copper grain, across a randomly oriented grain boundary facet.

The present Al-6Mg at 573K is a softening material. As shown in section 4.2, softer orientations accommodate considerably greater plastic strain and undergo fragmentation. In the present idealized microstructure, it is therefore reasonable to assume that the soft brass oriented grains develop greater plastic strains than the hard copper oriented grains. Thus, cases wherein the CRSS of the more deformed brass-oriented grains are smaller than that of the copper grains merit study. Accordingly, the CRSS of the slip systems in the near-brass grains, τ_{brass}, was set to one of the values in {0.1, 0.5, 1.0}, while that of the near-copper grains, τ_{copper}, was taken to be unity.

The binary-tree model polycrystal was subjected to plane strain deformation following the velocity gradient L_{ij}^{PSC} given by equation (1), to $\varepsilon = 0.20$, the critical strain of MSB

inception. Figure 9a shows the initial texture of the model polycrystal. The final textures of the model polycrystal corresponding to $\tau_{brass} = 1.0$, and $\tau_{brass} = 0.1$, are shown in figures 9b, and 9c, respectively. More quantitatively, figure 9d shows the evolution of the average Schmid factor in the near-brass and near-copper grains with progressing deformation. It is seen that while the Schmid factor of the near-brass grains remains practically unchanged for all τ_{brass} studied, that of the near-copper grains is quite sensitive to τ_{brass}. The near-copper grains thus undergo texture softening at a rate that increases rapidly with decreasing τ_{brass} (Banabic, 2016) . In short, while dynamic recovery (section 4.3) softens the initially soft-lattice oriented grains with deformation, texture softening does the same for the initially hard-lattice oriented grains. Once adequately texture softened, the initially hard grains may deform severely, and experience material softening though dynamic recovery. The initially hard grain will then set off the process of reorientation toward higher Schmid factor followed by intense deformation and softening amongst its hard neighbours in a cascading manner. This process must continue until the grains all along the diagonals of the specimen become sufficiently soft to undergo intense deformation, which marks the inception of the MSB. Thus, the kinetics of MSB inception is governed by the lattice rotation of the hard grains toward softer orientations.

In the binary-tree based model polycrystal, grains and sub-aggregates of grains deform while preserving traction and velocity continuity with their neighbouring grains and sub-aggregates (Mahesh, 2010). This causes all the grains, including the hard grains, to rotate. To illustrate this schematically, consider a pair of grains, as shown in figure 10e. Each grain is assumed to a possess a single slip system. Let the normal to the crystallographic slip planes and the slip direction be denoted $\vec{n}$, and $\vec{b}$, respectively. Under imposed simple shear, the Schmid factor of the softer grain with the horizontal slip plane is 1, while that of the harder grain with the vertical slip plane is 0. Compatible deformation of the two grains, as shown in figure 10e, will leave the lattice orientation of the soft grain unchanged, while rotating the

harder grain toward a softer orientation. If the intergranular continuity conditions between neighbouring grains were neglected in the polycrystal model, the deformation of the soft grains will leave the lattice orientations of both soft and hard grains unchanged. This is also illustrated in figure 10e.

In the classical Taylor (Taylor, 1938) model, grain interactions are neglected. The evolution of the average Schmid factor in the near-brass and near-copper grains predicted using the Taylor model are shown in figure 10f. The predicted Schmid factor evolution is independent of the value of τ_{brass} because in the Taylor model, each brass and copper grain must individually accommodate the macroscopically imposed strain, regardless of its CRSS. This renders the slip activity and the rotation of the two sets of grains independent of τ_{brass}. Further, the Taylor model predicts a gradual hardening of the soft brass orientation, and insignificant change in Schmid factor of the hard copper oriented grains. Comparing figures 10d and 10f indicates that polycrystal models that do not account for intergranular interactions cannot explain the lattice rotation that is essential for MSB formation.

4.5 Summary of the Microstructural Transitions

The combination of direct experimental observations, and modelling strongly point to the occurrence of the following qualitatively distinct stages from the onset of flow instability to MSB inception in the present Al-6Mg alloy deformed at 573K:

1. Strain localisation in isolated soft-oriented grains, aided by dynamic recovery is manifested macroscopically as the onset of flow instability and flow curve softening at $\varepsilon = 0.05$. The CRSS of such grains continues to decrease with localised deformation due to dynamic recovery. Substructural features associated with strain localisation within isolated single grains observed by Korbel et al. (1986) and Korbel and Martin (1986) pertain to this stage.

2. The hard-oriented neighbours of fragmenting grains, which are predominantly soft, rotate into softer orientations with progressing deformation through texture softening. As the hard grains approach softer orientations with rotation, they too develop large plastic strains, and undergo material softening due to dynamic recovery. Microbands extending across a few grains, observed by Korbel et al. (1986), and Korbel and Martin (1986) pertain to this stage.
3. Texture softening followed by material softening then progresses in a cascading manner to other grains, producing growing but isolated clusters of softening, intensely deforming grains.
4. At the critical strain of $\varepsilon = 0.20$, isolated clusters of highly deformed grains link up, and abruptly transform into a pair of continuous bands of heavily deformed and fragmented grains. The formation of this percolating network along the diagonals of the macroscopic specimen marks the inception of MSB. At this instant, macroscopically, the homogeneous deformation mode given by equation (1) transitions to the block shear mode given by equation (3).

5. Conclusions

1. Different aluminium alloys were subjected to plane strain indentations or 'strip tests' at 298K and 573K in a Gleeble^{TM} 3800. Only Al-6Mg deformed at 573K, showed clear formation of a macroscopic shear band or MSB and associated softening in stress-strain response. The MSB formation or propagation provided significantly higher ductility in Al-6Mg, though the final fracture also took place in the MSB.
2. The MSB was associated with marginally higher misorientation and hardness; but exhibited noticeably more grain elongation and fragmentation. It also showed higher recovery, as indicated by microstructures and more pop-in during nano-indentation.

3. Plasticity modelling, involving estimating velocity fields and deformation texture, indicated that a clear transition in strain mode was associated with MSB formation. In particular, physically, flow or shear localization followed about 20% homogeneous plane strain compression. Theoretical estimates, however, indicated flow instability at a smaller strain.
4. The inception of the physical MSBs coincided with the formation of a percolating network of highly fragmented grains that extended across the diagonals of the gage section. This network was comprised predominantly of grains of soft orientations. It is formed by the linkage of pre-existing soft grains and that of hard-grains rotated into soft orientations through texture softening. In other words, strain percolation appeared as the mechanism responsible for the inception of the physical macroscopic strain localization.
5. Finally, differential dynamic recovery, between soft and hard orientations, was quantitively established with the help of the X-ray resolution function, and was microstructurally shown in the MSB of 573K deformed Al-6Mg. It is thus proposed that differential dynamic recovery triggering strain percolation was responsible for the transition in velocity fields (from homogeneous to shear) – thus defining the origin of macroscopic shear band (MSB) formation.

6. Acknowledgment

The authors acknowledge support from the Indian Space Research Organization (ISRO). Support from the National Facility of Texture and OIM. CoEST (center for excellence in steel technology) Gleeble™ and Themis-300 TEM laboratories are also acknowledged.

7. References:

Aydıner, C.C., Telemez, M.A., 2014. Multiscale deformation heterogeneity in twinning magnesium investigated with in situ image correlation. International Journal of Plasticity 56, 203–218.

Backofen, W.A., 1973. Deformation Processing. Metallurgical Transaction 4, 1973–2679. https://doi.org/10.1016/B0-12-369401-9/00557-X

Banabic, D., 2016. Multiscale modelling in sheet metal forming. Springer.

Chang, Y.W., Asaro, R.J., 1981. An experimental study of shear localization in aluminum-copper single crystals. Acta Metallurgica 29, 241–257.

Considère, A., 1885. Mémoire sur l'emploi du fer et de l'acier, in: Annales Des Ponts Et Chaussées. pp. 574–775.

Dieter, G.E., Bacon, D., 1976. Mechanical metallurgy. McGraw-hill New York.

Dillamore, I.L., Roberts, J.G., Bush, A.C., 1979. Occurrence of shear bands in heavily rolled cubic metals. Metal Science 13, 73–77. https://doi.org/10.1179/msc.1979.13.2.73

Dodd, B., Bai, Y., 2014. Introduction to adiabatic shear localization (revised edition). World Scientific Publishing Company.

Efstathiou, C., Sehitoglu, H., Lambros, J., 2010. Multiscale strain measurements of plastically deforming polycrystalline titanium: Role of deformation heterogeneities. International Journal of Plasticity 26, 93–106.

Estrin, Y., Kubin, L.P., 1986. Local strain hardening and nonuniformity of plastic deformation. Acta Metallurgica 34, 2455–2464. https://doi.org/10.1016/0001-6160(86)90148-3

Fu, W., Li, Y., Hu, S., Sushko, P., Mathaudhu, S., 2022. Effect of loading path on grain misorientation and geometrically necessary dislocation density in polycrystalline aluminum under reciprocating shear. Computational Materials Science 205, 111221.

Green, A.P., 1951. XCII. A theoretical investigation of the compression of a ductile material between smooth flat dies. The London, Edinburgh, and Dublin Philosophical Magazine and Journal of Science 42, 900–918. https://doi.org/10.1080/14786445108561319

Guo, Y., Ruan, Q., Zhu, S., Wei, Q., Chen, H., Lu, J., Hu, B., Wu, X., Li, Y., Fang, D., 2019. Temperature rise associated with adiabatic shear band: causality clarified. Physical review letters 122, 015503.

Guo, Y., Ruan, Q., Zhu, S., Wei, Q., Lu, J., Hu, B., Wu, X., Li, Y., 2020. Dynamic failure of titanium: Temperature rise and adiabatic shear band formation. Journal of the Mechanics and Physics of Solids 135, 103811. https://doi.org/10.1016/j.jmps.2019.103811

Harren, S.V., Deve, H.E., Asaro, R.J., 1988a. Shear band formation in plane strain compression. Acta Metallurgica 36, 2435–2480.

Harren, S. V., Dève, H.E., Asaro, R.J., 1988b. Shear band formation in plane strain compression. Acta Metallurgica 36, 2435–2480. https://doi.org/10.1016/0001-6160(88)90193-9

Hart, E.W., 1967. Theory of the tensile test. Acta metallurgica 15, 351–355.

Harte, A., Atkinson, M., Preuss, M., Da Fonseca, J.Q., 2020. A statistical study of the relationship between plastic strain and lattice misorientation on the surface of a deformed Ni-based superalloy. Acta Materialia 195, 555–570.

Hill, R., 1950. The mathematical theory of plasticity, Clarendon. Oxford 613, 614.

Humphreys, F.J., Hatherly, M., 2012. Recrystallization and related annealing phenomena. Elsevier.

Jia, N., Eisenlohr, P., Roters, F., Raabe, D., Zhao, X., 2012. Orientation dependence of shear banding in face-centered-cubic single crystals. Acta Materialia 60, 3415–3434. https://doi.org/10.1016/j.actamat.2012.03.005

Johnson, W., Sowerby, R., Venter, R.D., 1982. Plane-Strain Slip-Line Fields for Metal-Deformation Processes, Plane-Strain Slip-Line Fields for Metal-Deformation Processes. Elsevier. https://doi.org/10.1016/c2013-0-10170-5

Jonas, J.J., Holt, R.A., Coleman, C.E., 1976. Plastic stability in tension and compression. Acta Metallurgica 24, 911–918.

Khatirkar, R., Vadavadagi, B., Shekhawat, S.K., Haldar, A., Samajdar, I., 2012. Orientation dependent recovery in interstitial free steel. ISIJ international 52, 884–893.

Korbel, A., 1990. The model of microshear banding in metals. Scripta Metallurgica et Materialia 24, 1229–1231.

Korbel, A., Embury, J.D., Hatherly, M., Martin, P.L., Erbsloh, H.W., 1986. Microstructural aspects of strain localization in Al□ Mg alloys. Acta Metallurgica 34, 1999–2009.

Korbel, A., Martin, P., 1986. Microscopic versus macroscopic aspect of shear bands deformation. Acta Metallurgica 34, 1905–1909.

Li, T.L., Gao, Y.F., Bei, H., George, E.P., 2011. Indentation Schmid factor and orientation dependence of nanoindentation pop-in behavior of NiAl single crystals. Journal of the Mechanics and Physics of Solids 59, 1147–1162. https://doi.org/10.1016/j.jmps.2011.04.003

Lodh, A., 2018. Microstructural Origin of Residual Stress. Doctor of Philosophy of the Indian Institute of Technology, Bombay, India and Monash University, Australia.

Lodh, A., Tak, T.N., Prakash, A., Guruprasad, P.J., Hutchinson, C., Samajdar, I., 2017. Relating Residual Stress and Substructural Evolution During Tensile Deformation of an Aluminum-Manganese Alloy. Metallurgical and Materials Transactions A:

Physical Metallurgy and Materials Science 48, 5317–5331. https://doi.org/10.1007/s11661-017-4280-x

Lodh, A., Tak, T.N., Prakash, A., Guruprasad, P.J., Keralavarma, S.M., Benzerga, A.A., Hutchinson, C., Samajdar, I., 2019. Microstructural Origin of Residual Stress Relief in Aluminum. Metallurgical and Materials Transactions A: Physical Metallurgy and Materials Science 50. https://doi.org/10.1007/s11661-019-05421-8

Loveday, M.S., Mahon, G.J., Roebuck, B., Lacey, A.J., Palmiere, E.J., Sellars, C.M., Van der Winden, M.R., 2006. Measurement of flow stress in hot plane strain compression tests. Materials at High Temperatures 23, 85–118.

Magagnosc, D.J., Lloyd, J.T., Meredith, C.S., Pilchak, A.L., Schuster, B.E., 2021. Incipient dynamic recrystallization and adiabatic shear bands in Ti–7Al studied via in situ X-ray diffraction. International Journal of Plasticity 141, 102992.

Mahesh, S., 2010. A binary-tree based model for rate-independent polycrystals. International Journal of Plasticity 26, 42–64. https://doi.org/10.1016/j.ijplas.2009.05.002

Mathur, P.S., Backofen, W.A., 1973. Mechanical Contributions To the Plane-Strain Deformation and Recrystallization Textures of Aluminum-Killed Steel. Metall Trans 4, 643–651. https://doi.org/10.1007/BF02643069

McQueen, H.J., Jonas, J.J., 1975. Recovery and recrystallization during high temperature deformation, in: Treatise on Materials Science & Technology. Elsevier, pp. 393–493.

Mostafaei, M.A., Kazeminezhad, M., 2012. Hot deformation behavior of hot extruded Al–6Mg alloy. Materials Science and Engineering: A 535, 216–221.

Mukunthan, K., Hawbolt, E.B., 1996. Modeling recovery and recrystallization kinetics in cold-rolled Ti-Nb stabilized interstitial-free steel. Metallurgical and Materials Transactions A 27, 3410–3423.

Needleman, A., Continuum, A.N., Appliquee, D.P., 1988. Continuum mechanics studies of plastic instabilities. Revue de Physique Appliquée 23, 585–593.

Pai, N., Prakash, A., Samajdar, I., Patra, A., 2022. Study of grain boundary orientation gradients through combined experiments and strain gradient crystal plasticity modeling. International Journal of Plasticity 156, 103360.

Paul, H., Driver, J.H., Tarasek, A., Wajda, W., Miszczyk, M.M., 2015. Mechanism of macroscopic shear band formation in plane strain compressed fine-grained aluminium. Materials Science and Engineering: A 642, 167–180.

Poliak, E.I., Jonas, J.J., 1996. A one-parameter approach to determining the critical conditions for the initiation of dynamic recrystallization. Acta materialia 44, 127–136.

Poliak, Jonas, 2003. Initiation of dynamic recrystallization in constant strain rate hot deformation. ISIJ international 43, 684–691.

Prakash, A., Tak, T.N., Anand, A., Pai, N.N., Narayana Murty, S.V.S., Singh, C.V., Guruprasad, P.J., Samajdar, I., 2022a. Mechanistic Origin of Orientation-Dependent Substructure Evolution in Aluminum and Aluminum-Magnesium Alloys. Metallurgical and Materials Transactions A 1–19.

Prakash, A., Tak, T.N., Anand, A.B.U., Pai, N.N., 2022b. Mechanistic Origin of Orientation-Dependent Substructure Evolution in Aluminum and Aluminum-Magnesium Alloys. Metallurgical and Materials Transactions A 53, 2689–2707. https://doi.org/10.1007/s11661-022-06698-y

Prakash, A., Tak, T.N., Pai, N.N., Murty, S.V.S.N., Guruprasad, P.J., Doherty, R.D., Samajdar, I., 2021. Slip band formation in low and high solute aluminum: a combined experimental and modeling study. Modelling and Simulation in Materials Science and Engineering 29. https://doi.org/10.1088/1361-651X/ac3369

Raabe, D., Sachtleber, M., Zhao, Z., Roters, F., Zaefferer, S., 2001. Micromechanical and macromechanical effects in grain scale polycrystal plasticity experimentation and simulation. Acta materialia 49, 3433–3441.

Raveendra, S., Kanjarla, A.K., Paranjape, H., Mishra, S.K., Mishra, S., Delannay, L., Samajdar, I., Van Houtte, P., 2011. Strain mode dependence of deformation texture developments: microstructural origin. Metallurgical and Materials Transactions A 42, 2113–2124.

Reimers, W., Dupke, R., 1995. Procedures for Residual Stress Analysis in Textured and in Coarse Grained Materials. Textures and Microstructures 23, 173–183. https://doi.org/10.1155/tsm.23.173

Reyne, B., Moës, N., Manach, P.-Y., 2020. A persistent modal plastic model for instabilities in Al–Mg alloys with 1D application. International Journal of Plasticity 131, 102713.

Romhanji, E., Dudukovska, M., Glišić, D., 2002. The effect of temperature on strain-rate sensitivity in high strength Al–Mg alloy sheet. Journal of materials processing technology 125, 193–198.

Semiatin, S. L., Lahoti, G. D., & Oh, S.I., 1983. The occurrence of shear bands in metalworking, in: Material Behavior Under High Stress and Ultrahigh Loading Rates. Springer, Boston, pp. 119–159.

Semiatin, S.L., Jonas, J.J., 1984. Formability and workability of metals: plastic instability and flow localization. American Society for Metals, 1984, 299.

Semiatin, S.L., Lahoti, G.D., 1982. The occurrence of shear bands in isothermal, hot forging. Metallurgical Transactions A 13, 275–288. https://doi.org/10.1007/BF02643318

Semiatin, S.L., Lahoti, G.D., 1981. Deformation and unstable flow in hot forging of Ti-6Ai-2Sn-4Zr-2Mo-0.1 Si. Metallurgical Transactions A 12, 1705–1717.

Singh, J., Mahesh, S., Roy, S., Kumar, G., Srivastava, D., Dey, G.K., Saibaba, N., Samajdar, I., 2017. Temperature dependence of work hardening in sparsely twinning zirconium. Acta Materialia 123, 337–349. https://doi.org/10.1016/j.actamat.2016.10.049

Standard Practice for Compression Tests of Metallic Materials at Elevated Temperatures with Conventional or Rapid Heating Rates and Strain Rates [WWW Document], n.d. URL https://www.astm.org/e0209-18.html (accessed 2.27.23).

Sudharshan Phani, P., Oliver, W.C., 2020. Critical examination of experimental data on strain bursts (pop-in) during spherical indentation. Journal of Materials Research 35, 1028–1036. https://doi.org/10.1557/jmr.2019.416

Sudharshan Phani, P., Oliver, W.C., 2019. A critical assessment of the effect of indentation spacing on the measurement of hardness and modulus using instrumented indentation testing. Materials and Design 164, 107563. https://doi.org/10.1016/j.matdes.2018.107563

Sudharshan Phani, P., Oliver, W.C., Pharr, G.M., 2021. Measurement of hardness and elastic modulus by load and depth sensing indentation: Improvements to the technique based on continuous stiffness measurement. Journal of Materials Research 36, 2137–2153. https://doi.org/10.1557/s43578-021-00131-7

Tang, B., Xiang, L., Cheng, L., Liu, D., Kou, H., Li, J., 2018. The formation and evolution of shear bands in plane strain compressed nickel-base superalloy. Metals 8, 141.

Taylor, G.I., 1938. Plastic strain in metals. our. Inst. Metals. 62, 307–324.

Thool, K., Patra, A., Fullwood, D., Krishna, K.V.M., Srivastava, D., Samajdar, I., 2020. The role of crystallographic orientations on heterogeneous deformation in a zirconium alloy: A combined experimental and modeling study. International Journal of Plasticity 133, 102785. https://doi.org/10.1016/j.ijplas.2020.102785

Üçel, İ.B., Kapan, E., Türkoğlu, O., Aydıner, C.C., 2019. In situ investigation of strain heterogeneity and microstructural shear bands in rolled Magnesium AZ31. International Journal of Plasticity 118, 233–251.

Vadavadagi, B.H., Shekhawat, S.K., Samajdar, I., Narasimhan, K., 2016. Forming limit curves in low-carbon steels: improved prediction by incorporating microstructural evolution. The International Journal of Advanced Manufacturing Technology 86, 1027–1036.

Vanhoutte, P., L, D., 1999. The influence of crystallographic texture on diffraction measurements of residual stress. Acta.Metall.Mater 41, 323–336.

Verlinden, B., Driver, J., Samajdar, I., Doherty, R.D., 2007a. Thermo-mechanical processing of metallic materials. Elsevier.

Verlinden, B., Driver, J., Samajdar, I., Doherty, R.D., 2007b. Thermo-mechanical processing of metallic materials. Elsevier.

Wagner, P., Engler, O., Lücke, K., 1995. Formation of Cu-type shear bands and their influence on deformation and texture of rolled fcc ${$112$}$\textless 111\textgreater single crystals. Acta Metallurgica et Materialia 43, 3799–3812.

Wang, M.G., Ngan, A.H.W., 2004. Indentation strain burst phenomenon induced by grain boundaries in niobium. Journal of Materials Research 19, 2478–2486. https://doi.org/10.1557/JMR.2004.0316

Withers, P.J.J., Bhadeshia, H.K.D.H.K.D.H., 2001. Residual stress Part 1 – Measurement techniques. Materials Science and Technology 17, 355–365. https://doi.org/10.1179/026708301101509980

Xu, J., Holmedal, B., Hopperstad, O.S., Mánik, T., Marthinsen, K., 2022. Dynamic strain ageing in an AlMg alloy at different strain rates and temperatures: experiments and constitutive modelling. International Journal of Plasticity 151, 103215.

Yerra, S.K., Verlinden, B., Van Houtte, P., 2005. On crystallographic texture of as-drawn doped-W wires, in: Materials Science Forum. Trans Tech Publ, pp. 913–918.

Yuzbekova, D., Mogucheva, A., Zhemchuzhnikova, D., Lebedkina, T., Lebyodkin, M., Kaibyshev, R., 2017. Effect of microstructure on continuous propagation of the Portevin–Le Chatelier deformation bands. International Journal of Plasticity 96, 210–226.

Zha, M., Zhang, H., Jia, H., Gao, Y., Jin, S., Sha, G., Bjørge, R., Mathiesen, R.H., Roven, H.J., Wang, H., 2021. Prominent role of multi-scale microstructural heterogeneities on superplastic deformation of a high solid solution Al–7Mg alloy. International Journal of Plasticity 146, 103108.

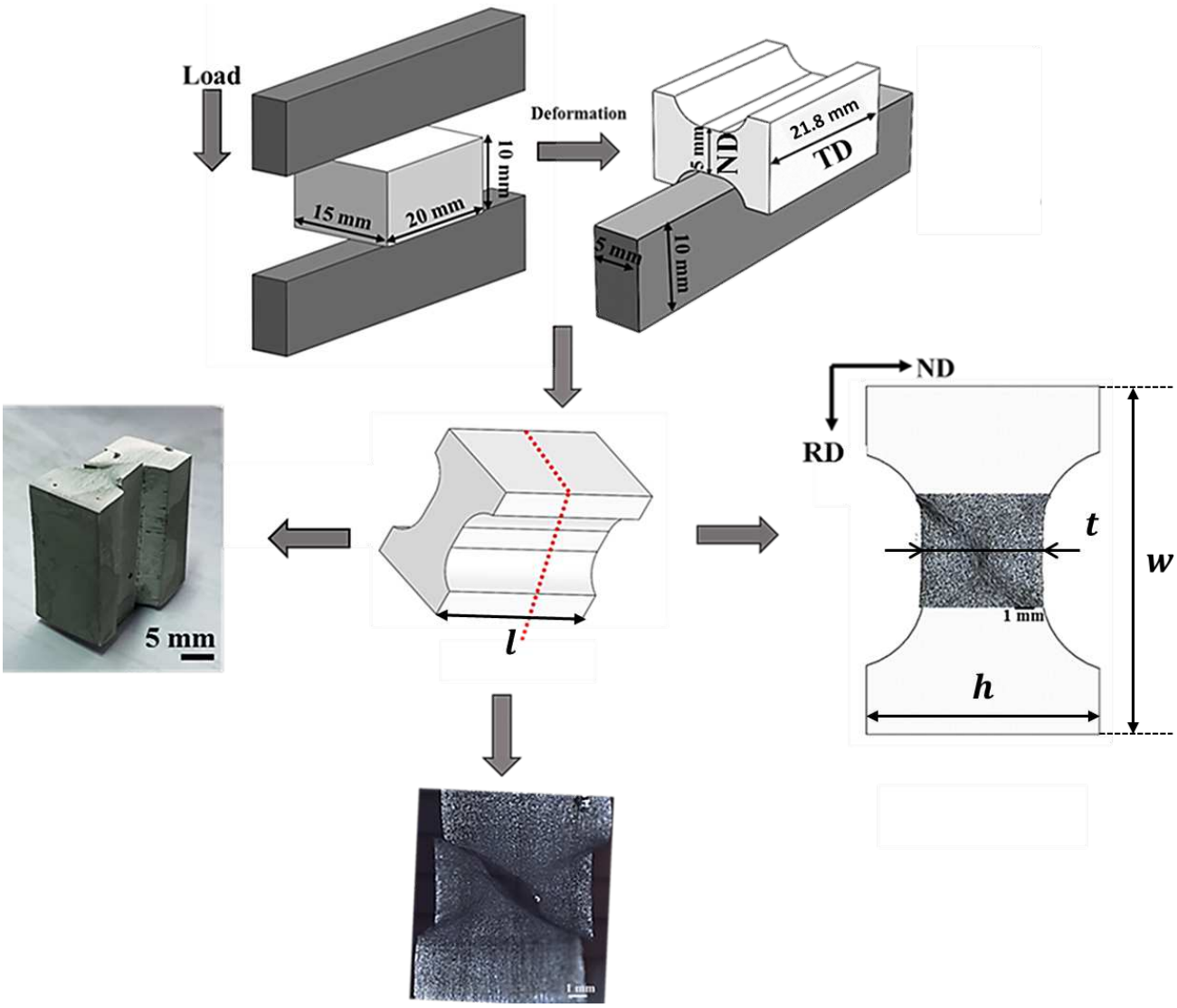
Load
Deformation
10 mm
15 mm
20 mm
21.8 mm
TD
ND
5 mm
10 mm
5 mm
ND
RD
t
w
1 mm
h
l
1 mm

(a)

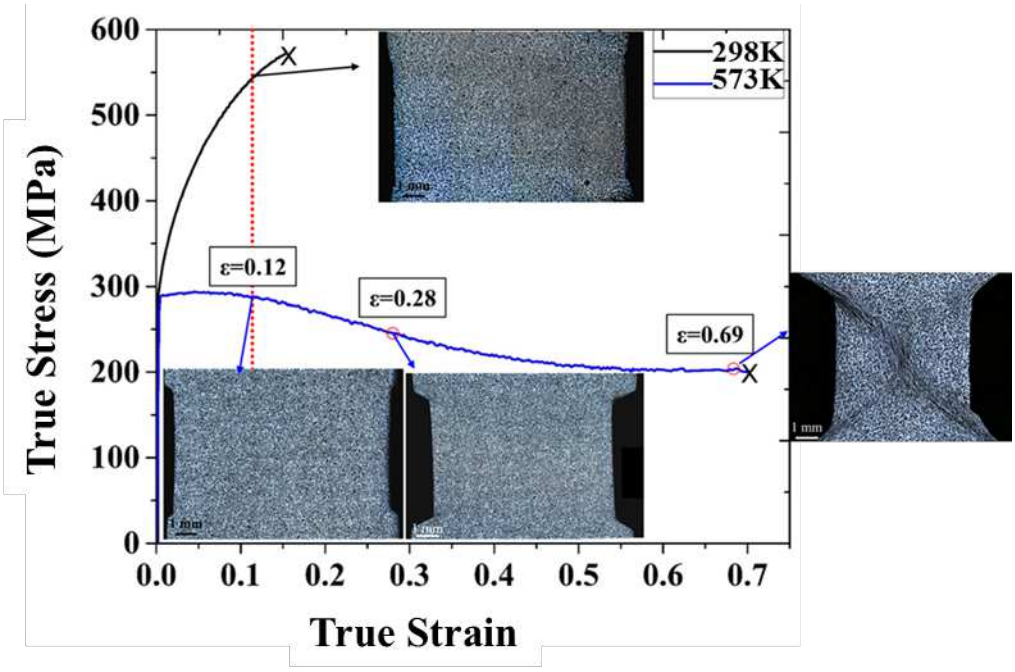
True Stress (MPa)
True Strain
298K
573K
ε=0.12
ε=0.28
ε=0.69
0
100
200
300
400
500
600
0.0
0.1
0.2
0.3
0.4
0.5
0.6
0.7

(b)

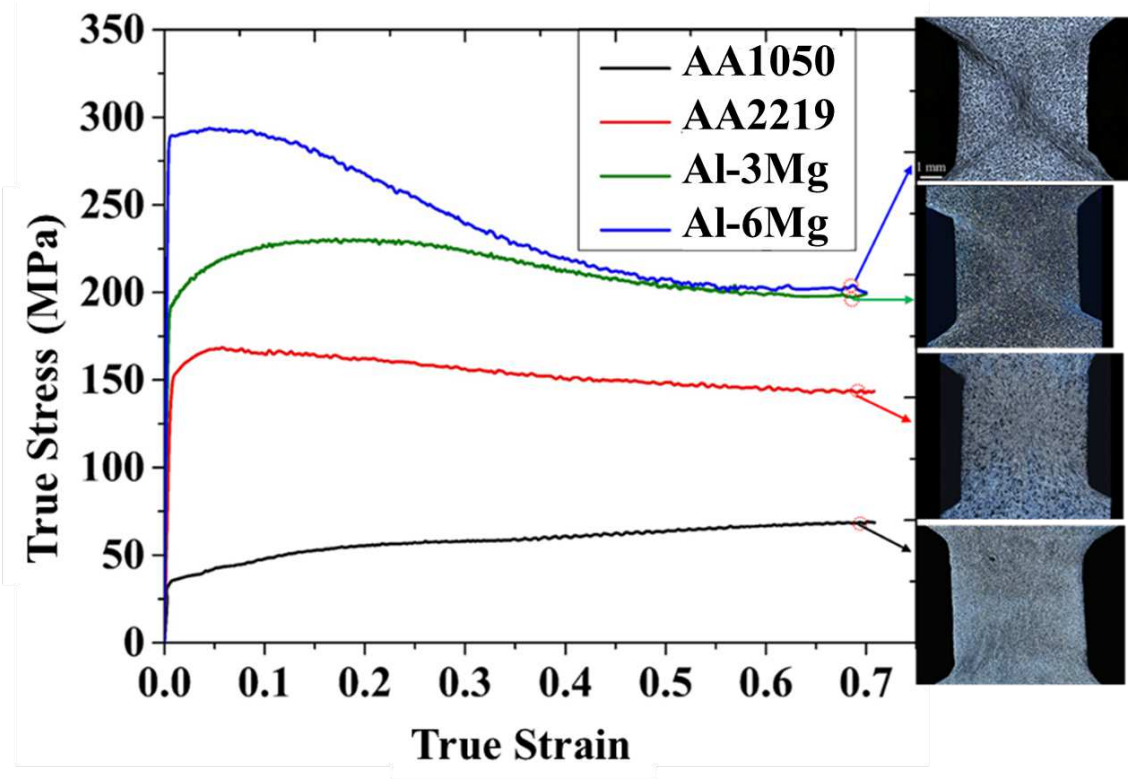

(c)

Figure 1: (a) Schematic of 'strip' testing (Verlinden et al. 2007b) or plane strain indentation in a deformation simulator (Gleeble™). It is to be noted here that the deformed dimensions are specifically correct for a true strain of 0.69. Images of the as-deformed (with macroscopic shear banding or MSB) and as-fractured specimens of Al-6Mg are included. For further details on post strip testing geometries, the reader may refer to Appendix A. True stress (σ) versus true strain (ε) responses of (b) Al-6Mg deformed at 298K and 573K and (c) different aluminum alloys deformed at 573K. Selected specimen cross sections, indicating MSB formation or otherwise, are shown.

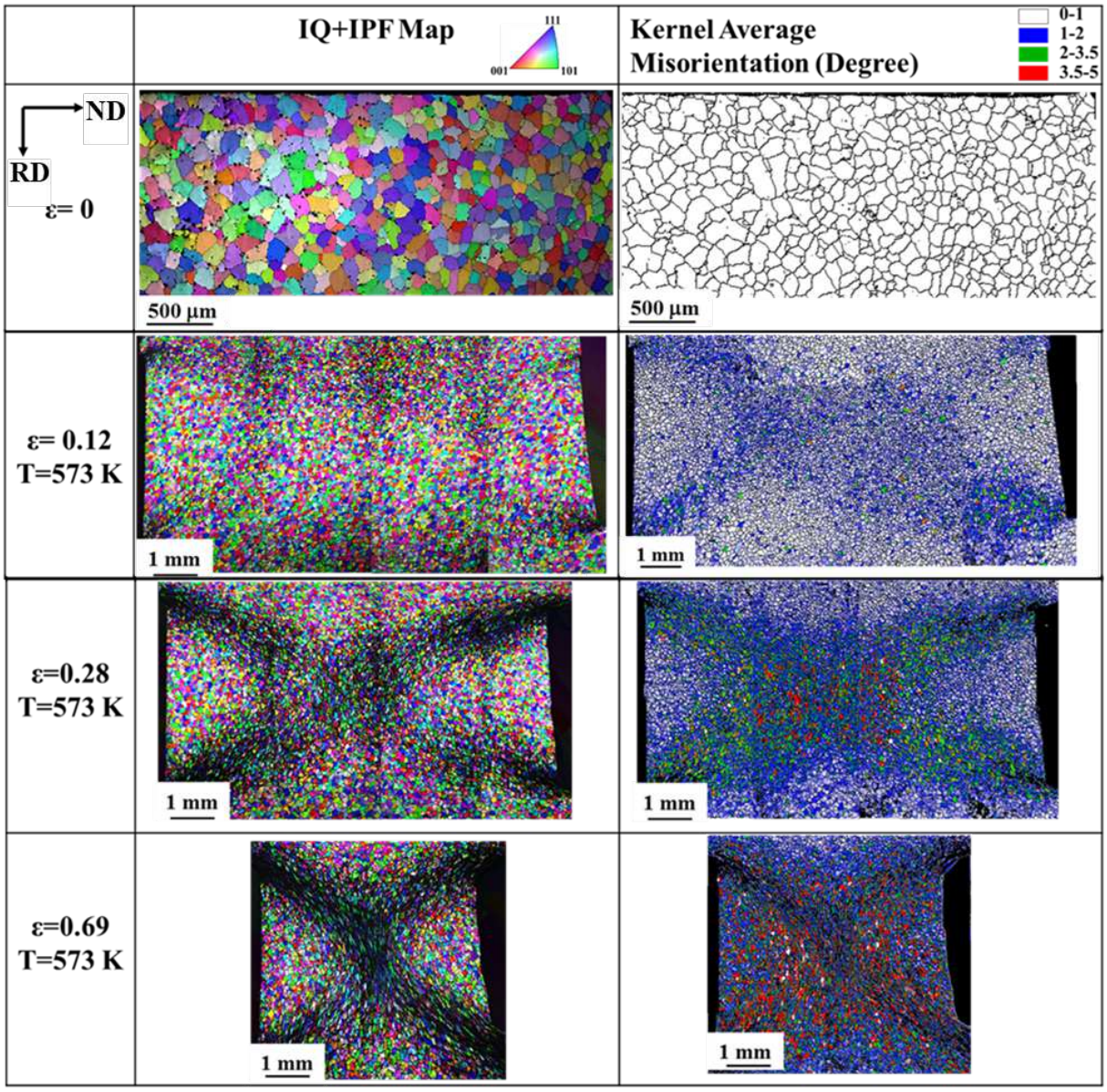
IQ+IPF Map
111
001
101
Kernel Average
Misorientation (Degree)
0-1
1-2
2-3.5
3.5-5
ND
RD
ε= 0
500 µm
500 µm
ε= 0.12
T=573 K
1 mm
1 mm
ε=0.28
T=573 K
1 mm
1 mm
ε=0.69
T=573 K
1 mm
1 mm

(a)

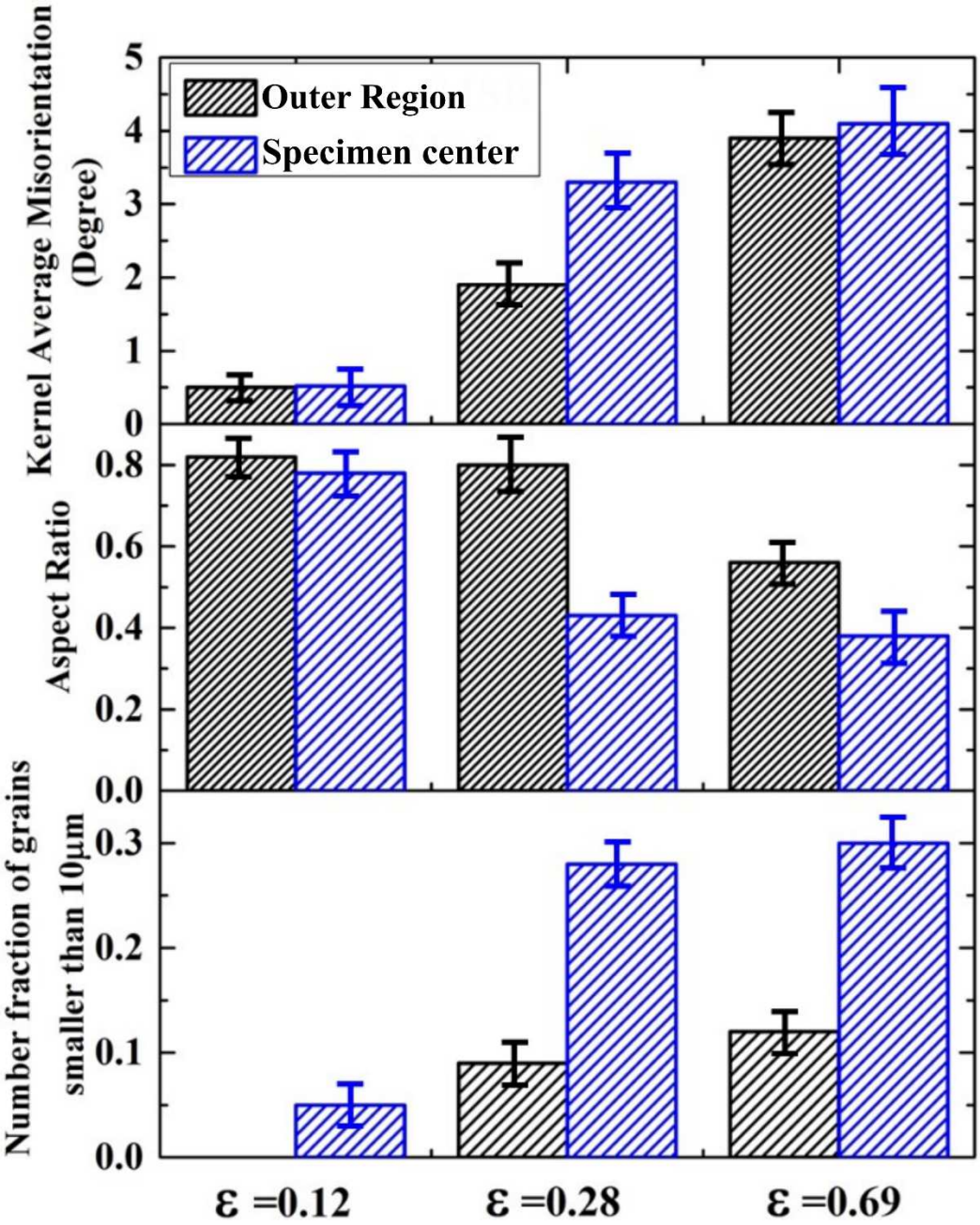
Kernel Average Misorientation (Degree)
Outer Region
Specimen center
Aspect Ratio
Number fraction of grains smaller than 10μm
ε =0.12
ε =0.28
ε =0.69

(b)

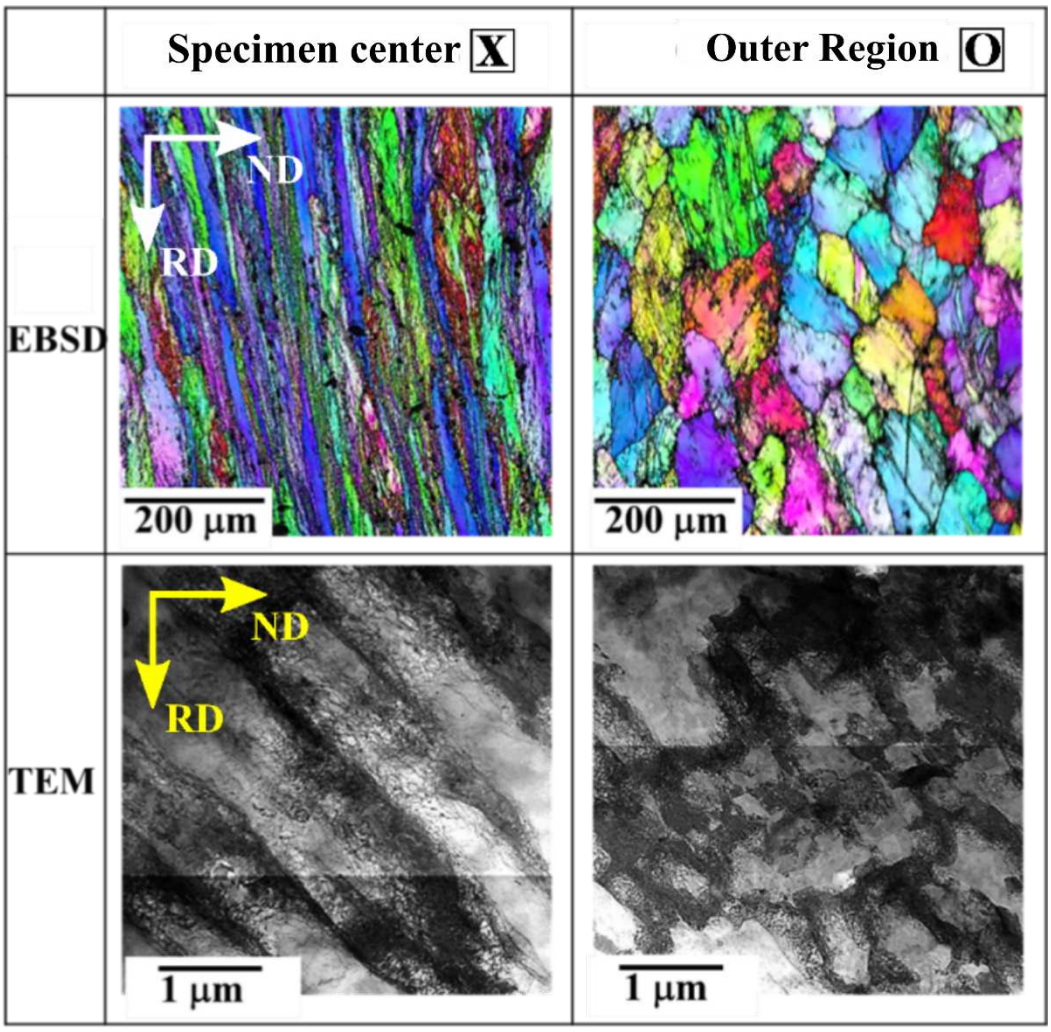

(c)

Figure 2: Microstructures of MSB formation, in Al-6Mg, subjected to 'strip' testing at 573K. (a) Electron Backscattered Diffraction (EBSD) Inverse Pole Figure (IPF) and Kernel Average Misorientation (KAM) maps of specimen cross-sections for different imposed plastic strains (ε). (b) Development of KAM, grain aspect ratio and number fraction of grains smaller than 10 μm shown from both inside and outside the MSB. (c) EBSD and transmission electron microscopy (TEM) images for ε=0.69 taken from inside (X) and outside (O) the MSB.

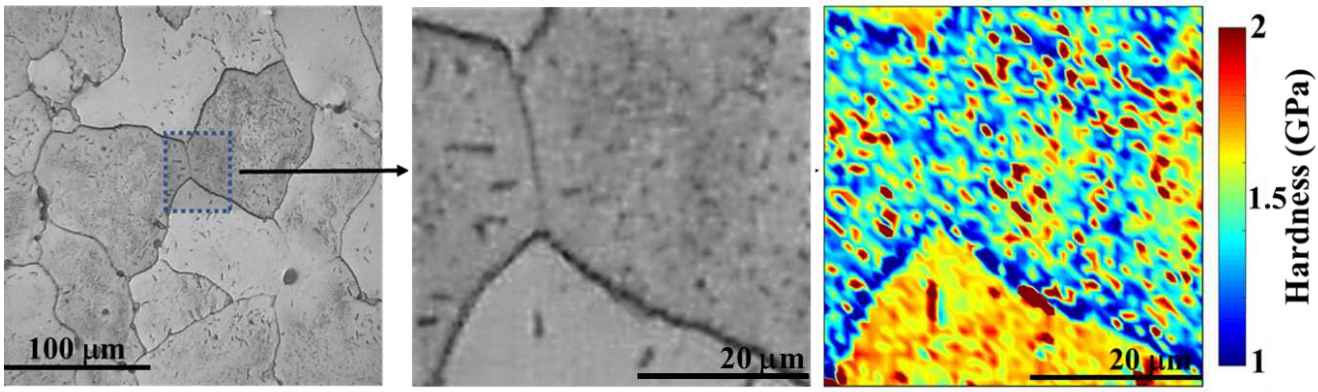
100 µm
20 µm
20 µm
2
1.5
1
Hardness (GPa)

(a)

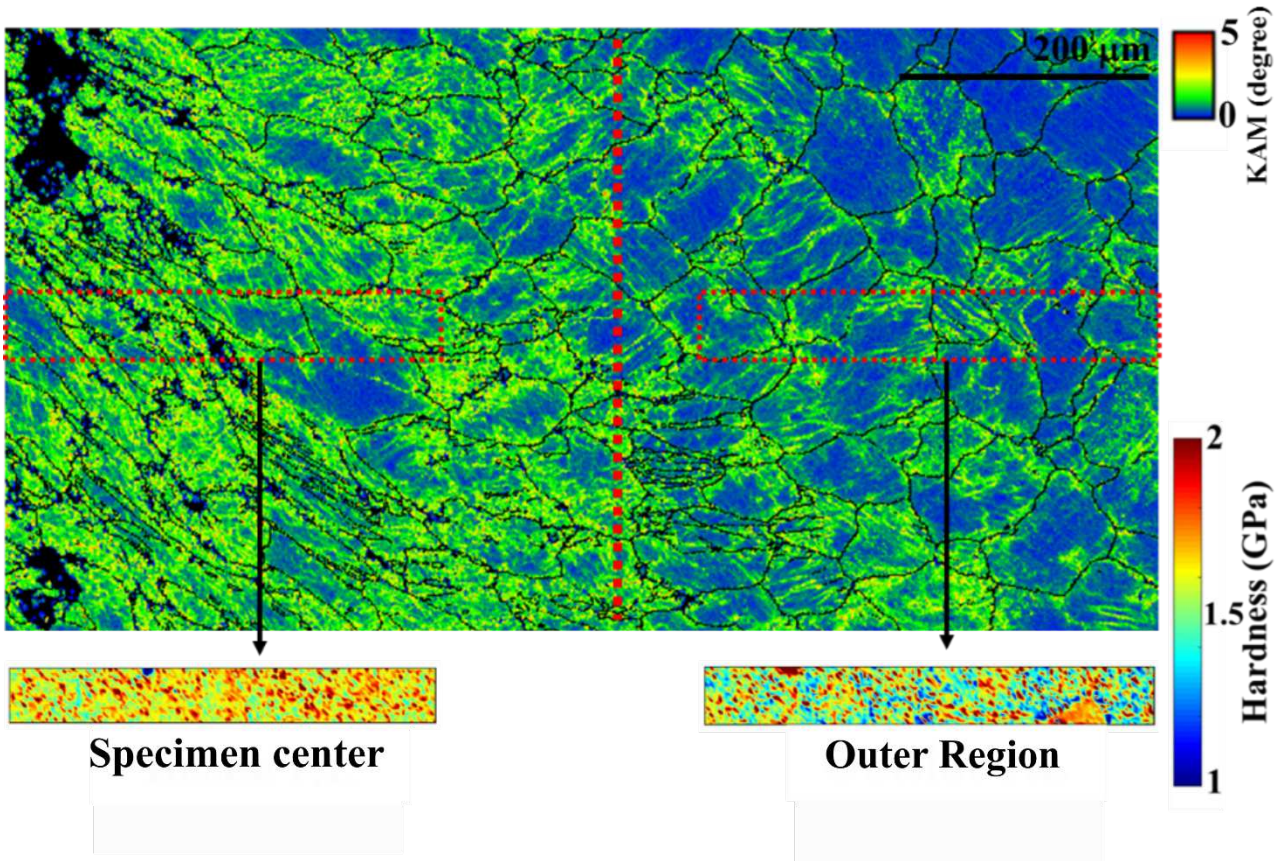
200 µm
5
0
KAM (degree)
2
1.5
1
Hardness (GPa)
Specimen center
Outer Region

(b)

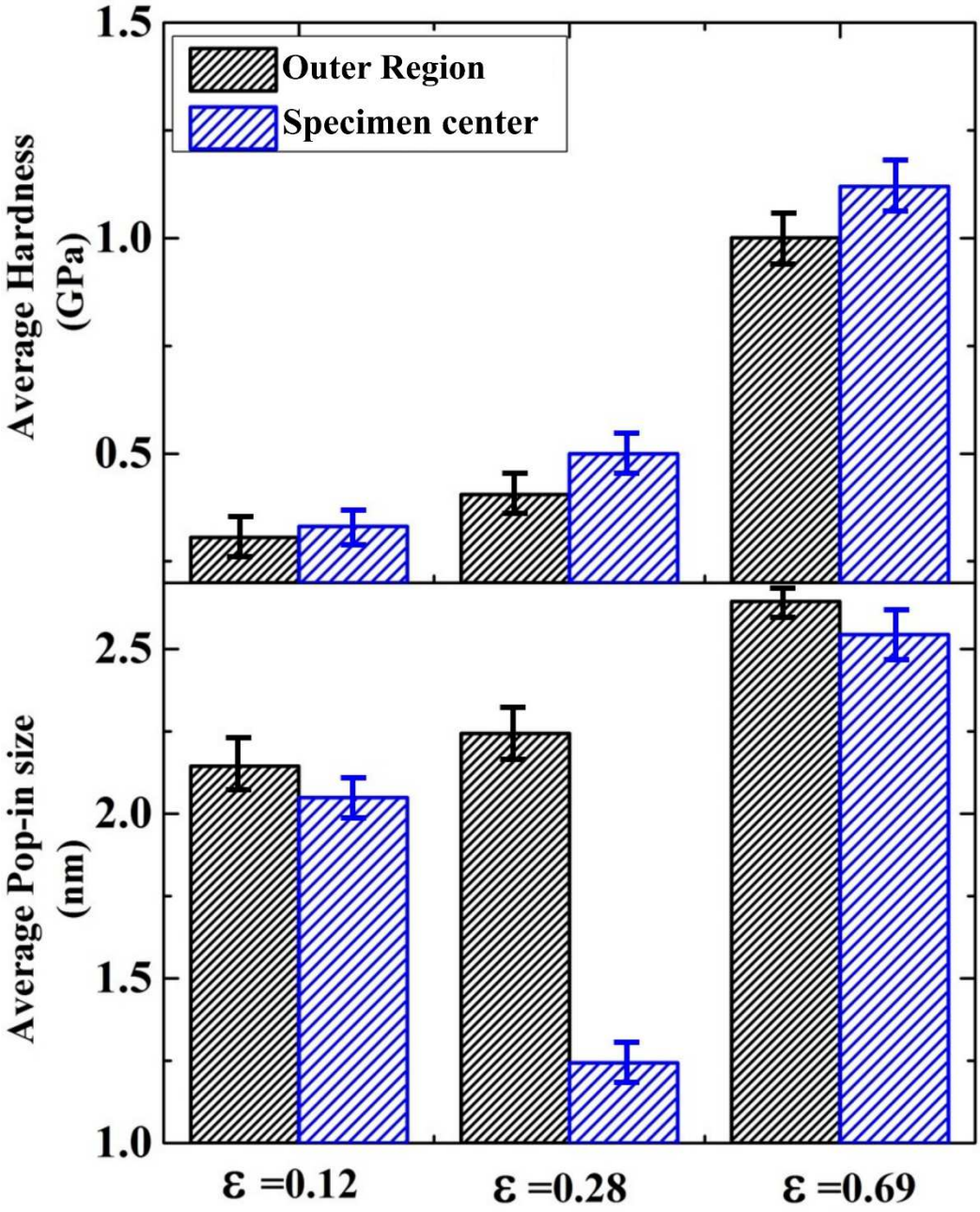

(c)

Figure 3: (a) Hardness map and corresponding SEM image for undeformed Al-6Mg. (b) KAM and hardness maps for Al-6Mg deformed at 573K to ε= 0.28. Hardness maps were taken from inside and outside the MSB. (c) Data on average hardness and pop-in size from inside and outside the MSB.

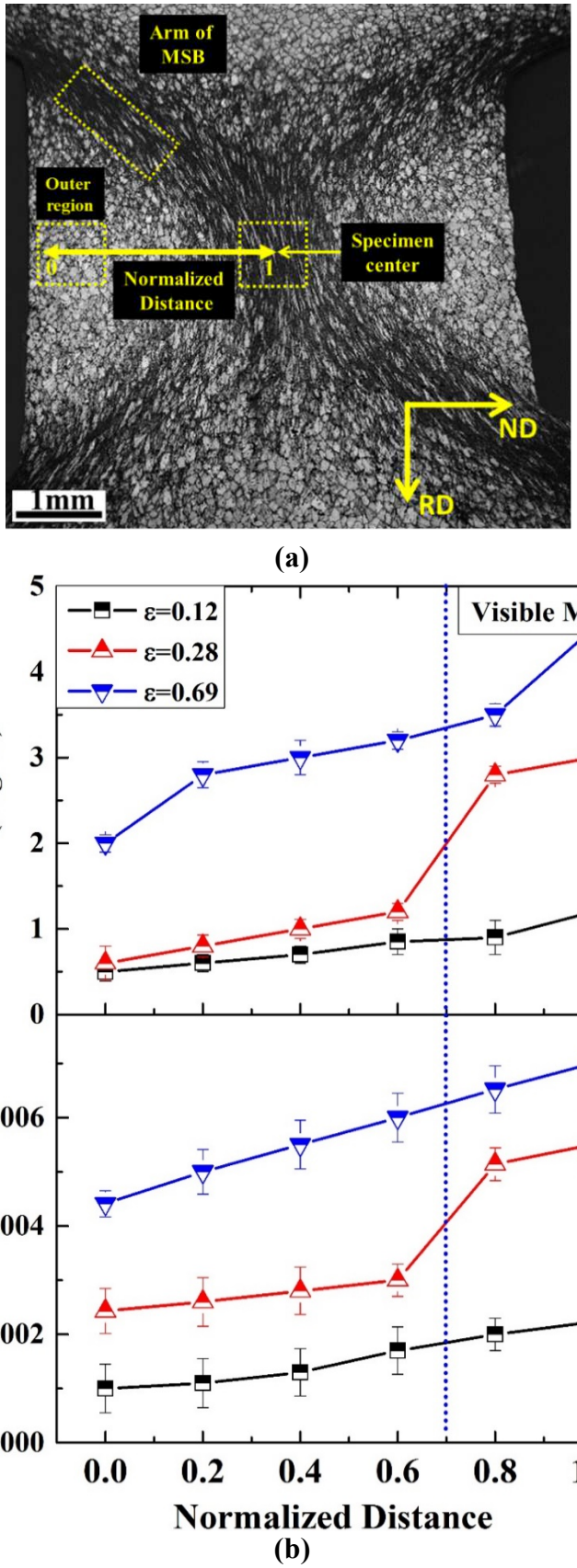

Figure 4: (a) Microstructure of a deformed sample showing normalized distance and different regions (inside, centre, and arm of the MSB; and outside the MSB). (b) KAM and Residual strain along the rolling direction (RD) versus normalized distance.

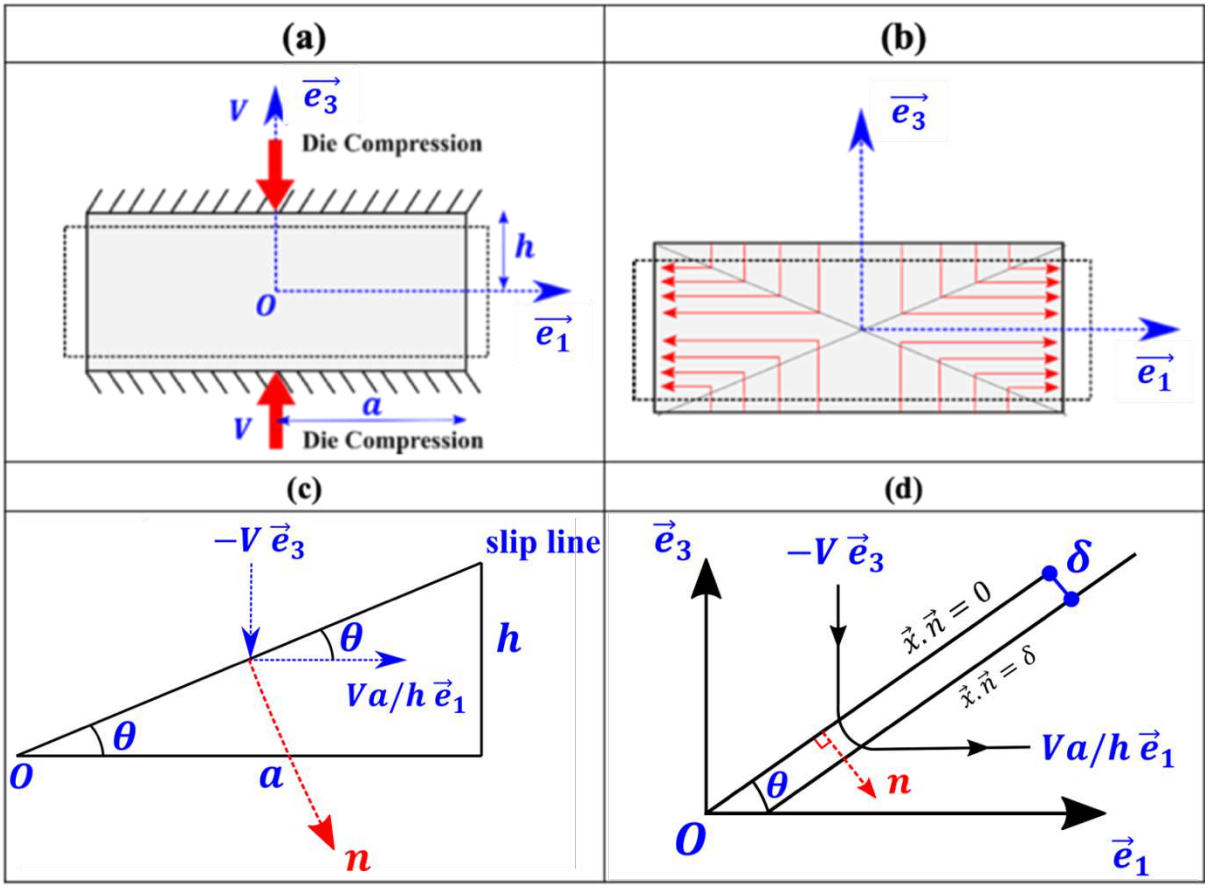

Figure 5: Schematic illustrating (a) homogeneous plane strain compression (PSC), and (b) localized shear deformation along the diagonals. Both represent RD-ND gauge region or the LT section. Red lines in (b) indicate a simple flow field. (c) The trace of a material point through the slip line (see equations (2) and (3) for further details). (d) A slip zone of width δ, constructed to establish continuity within the slip line.

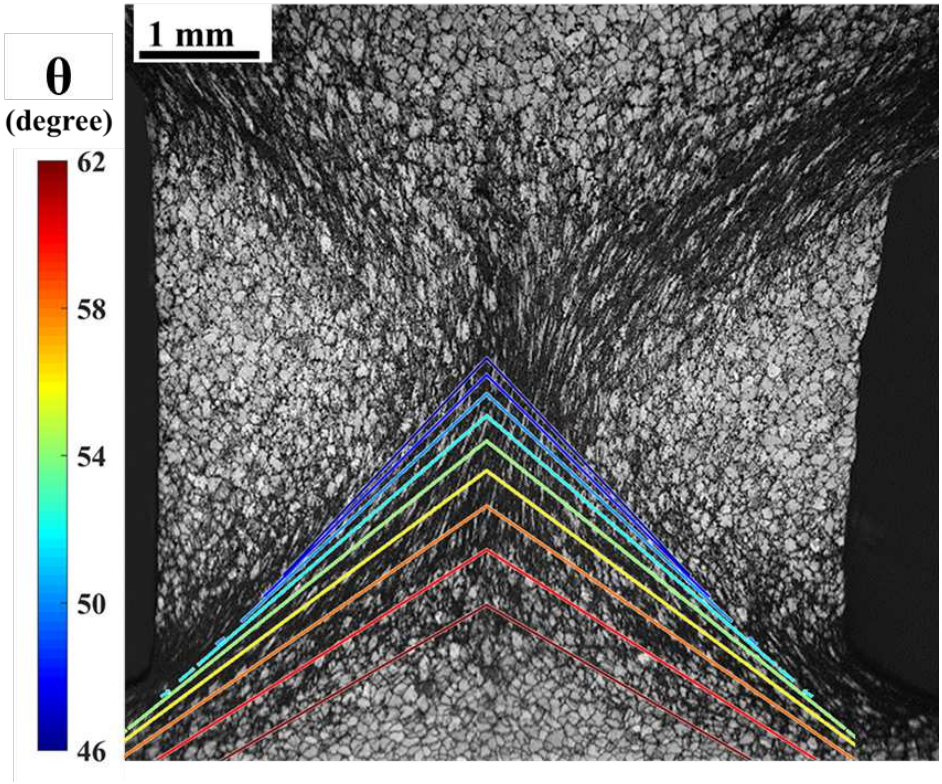

(a)

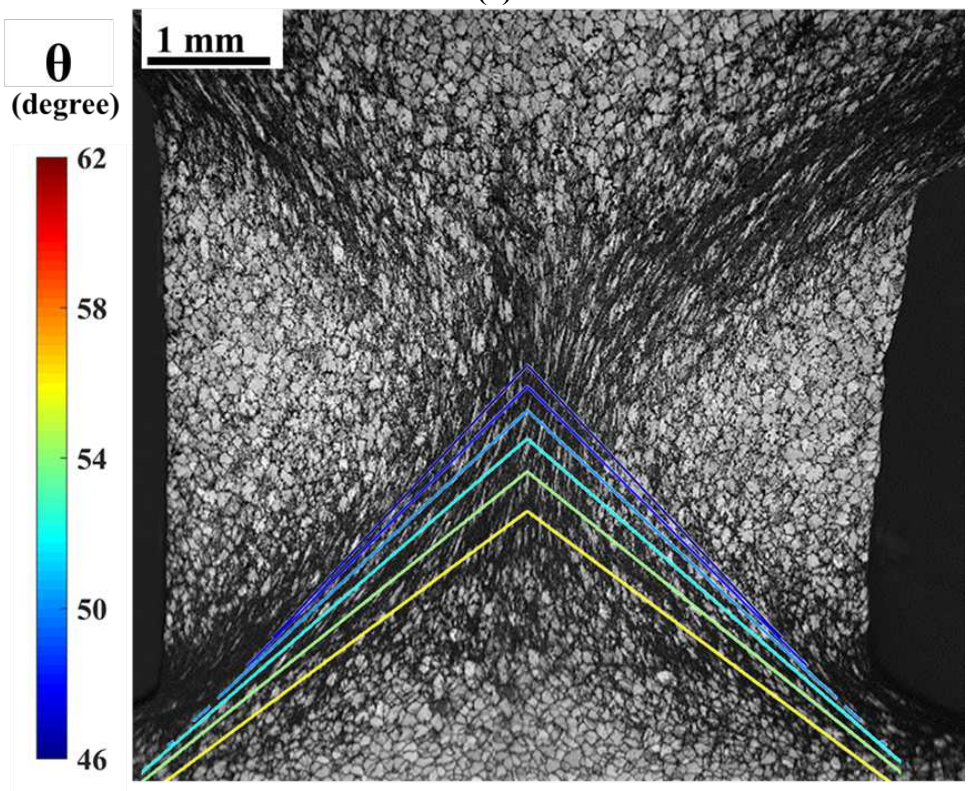

(b)

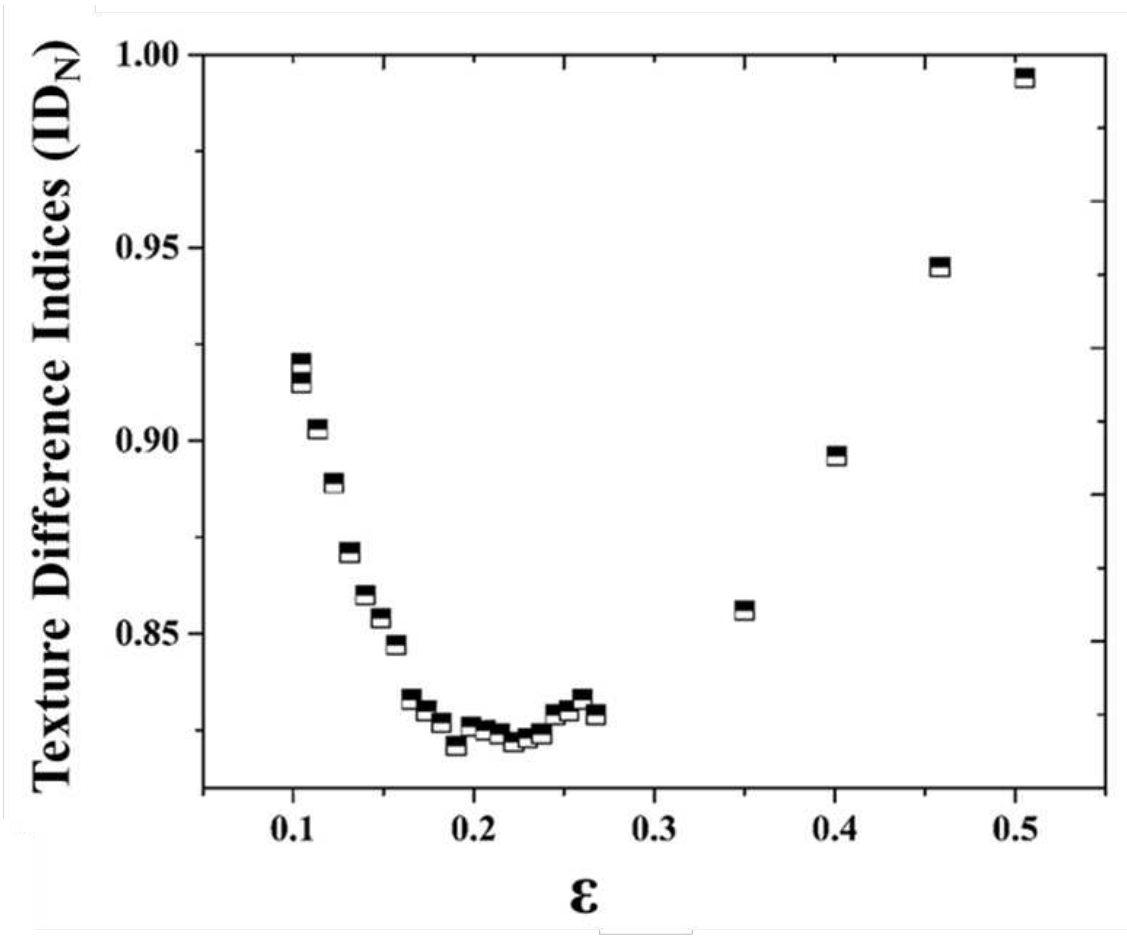
Texture Difference Indices (ID_N)
1.00
0.95
0.90
0.85
0.1
0.2
0.3
0.4
0.5
ε

(c)

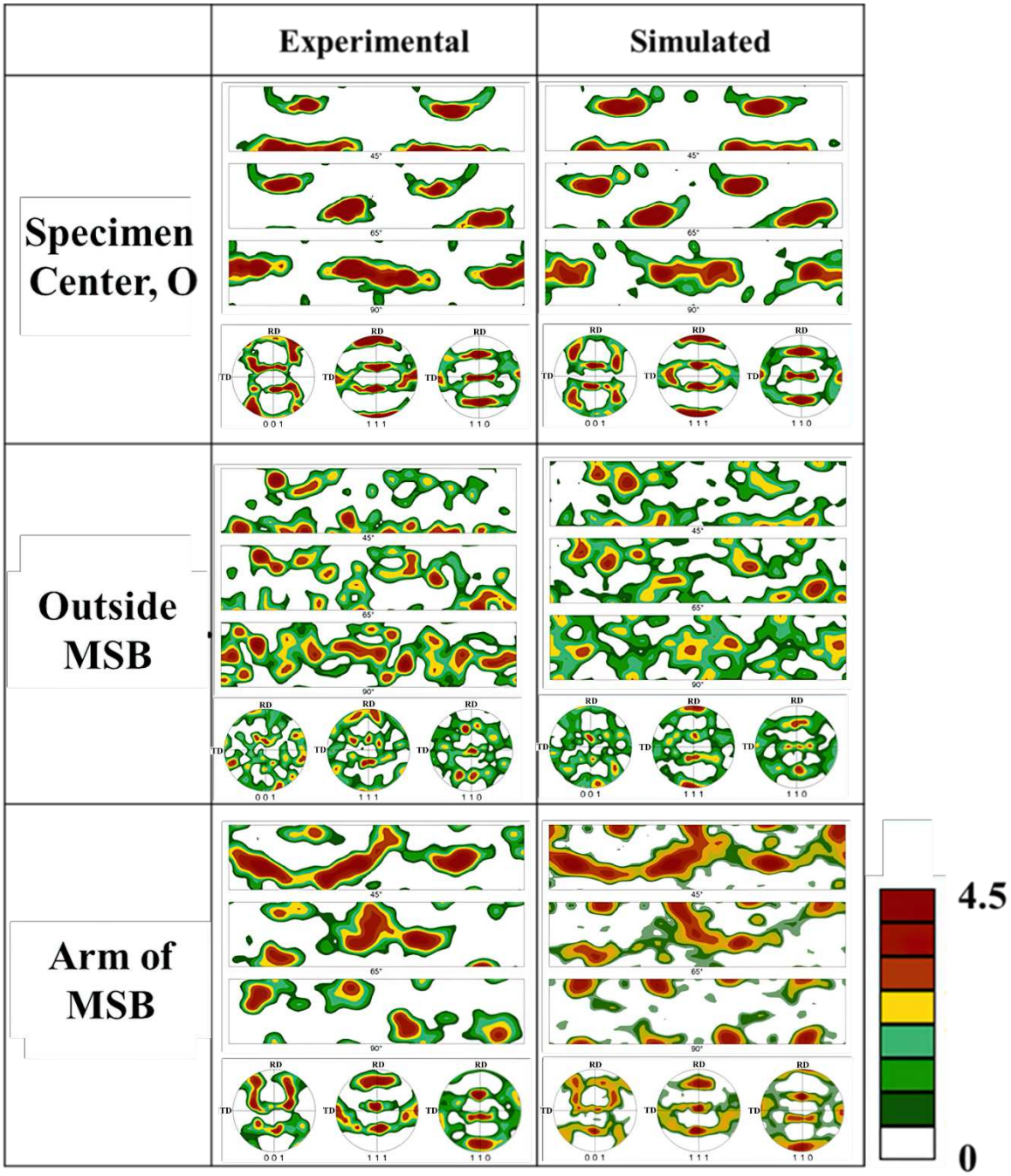

(d)

Figure 6: Schematic of simulated slip lines, as estimated from plasticity modelling. These are imposed on experimental MSB of Al-6Mg, subjected to PSC ε= 0.69 at 573K. Plasticity simulations were conducted assuming localized shear (a) from the beginning and (b) after ε=0.2. (c) Texture difference ID_N (eq. (12)) between experimental and simulated textures. (d) Experimental and simulated textures for Al-6Mg deformed at 573K to ε = 0.69 in the different regions.

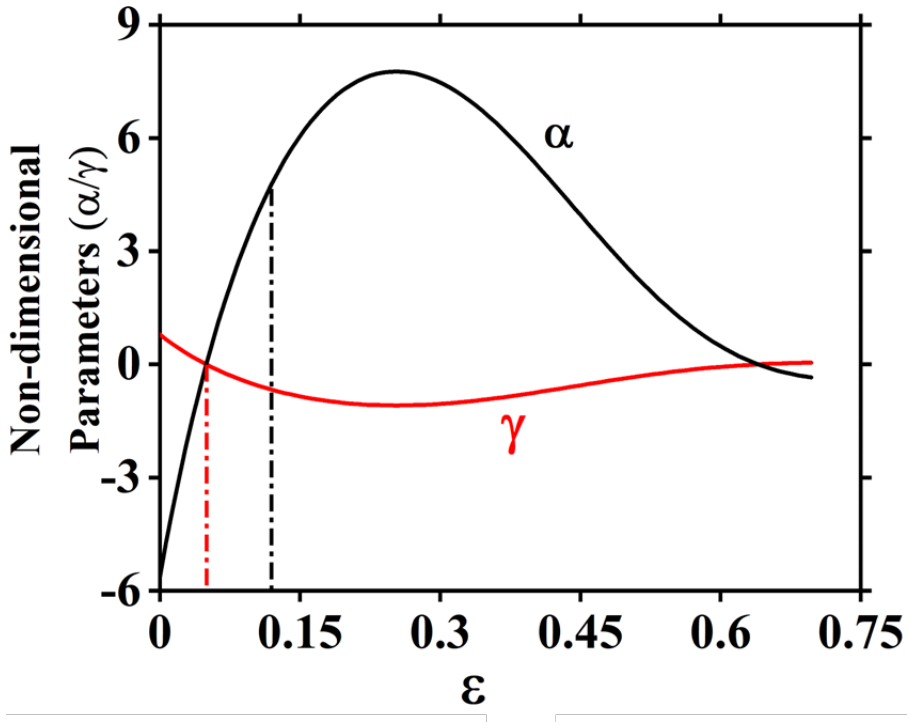
Non-dimensional Parameters (α/γ)
9
6
3
0
-3
-6
0
0.15
0.3
0.45
0.6
0.75
ε
α
γ

(a)

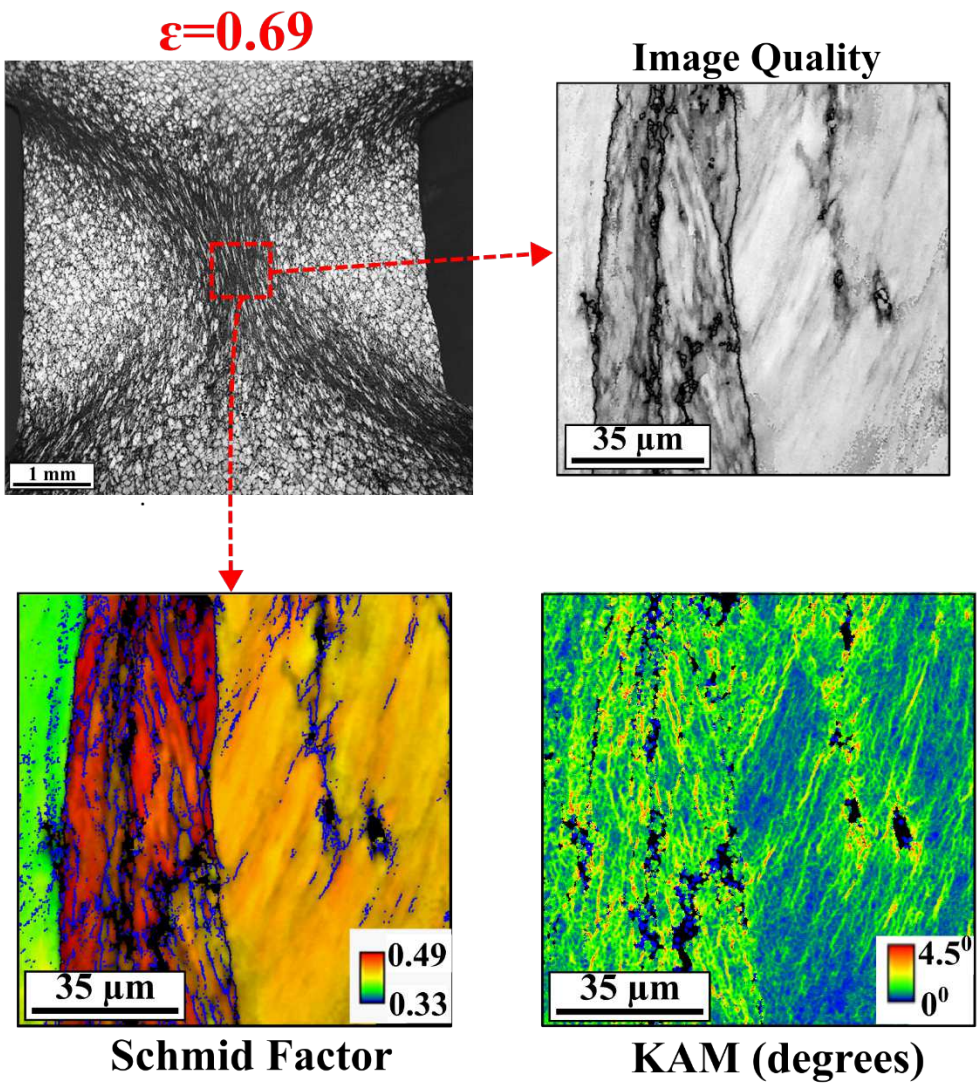
ε=0.69
1 mm
Image Quality
35 µm
35 µm
0.49
0.33
Schmid Factor
35 µm
4.5⁰
0⁰
KAM (degrees)

(b)

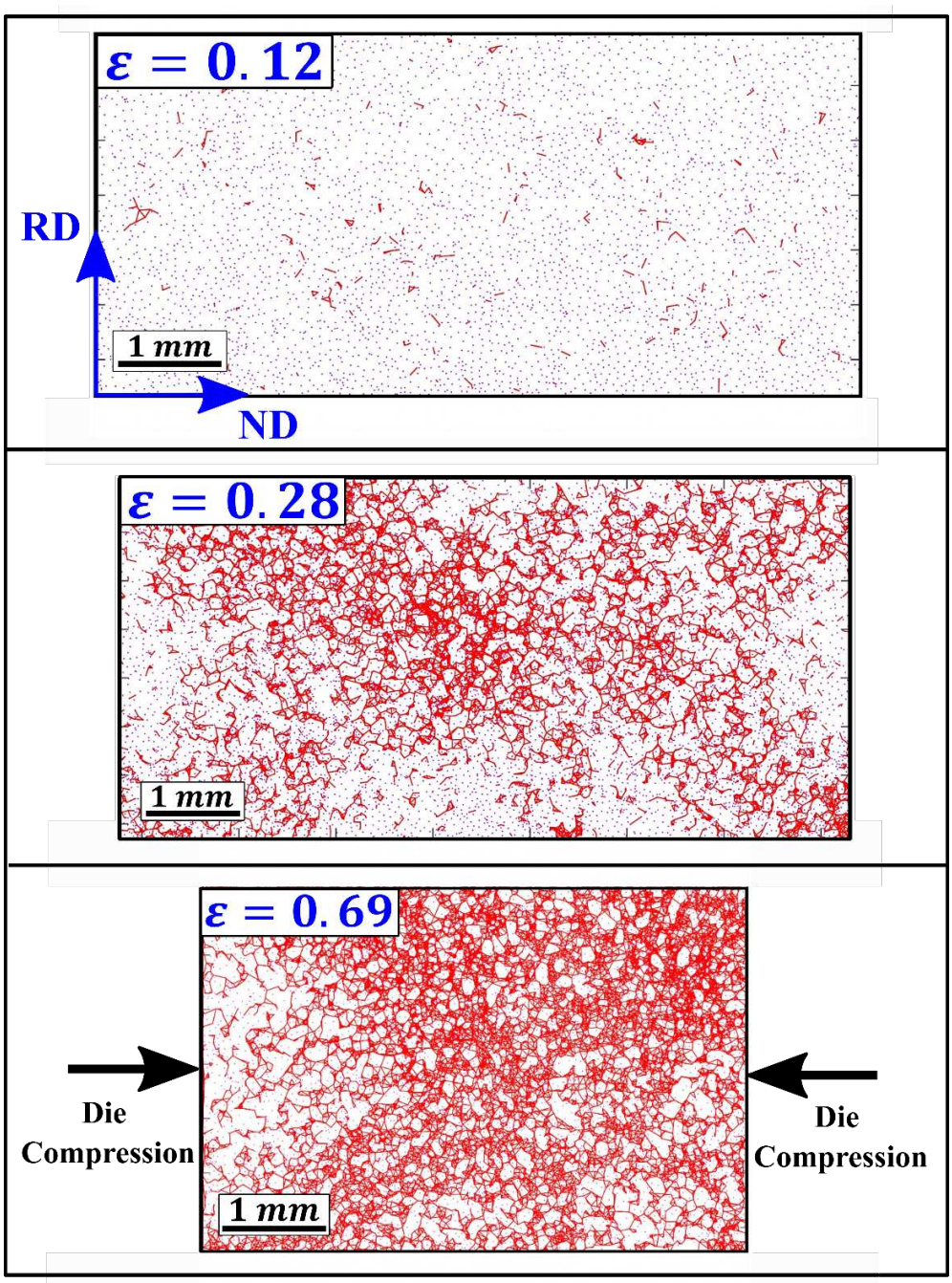
ε = 0.12
RD
1 mm
ND
ε = 0.28
1 mm
ε = 0.69
Die
Compression
1 mm
Die
Compression

(c)

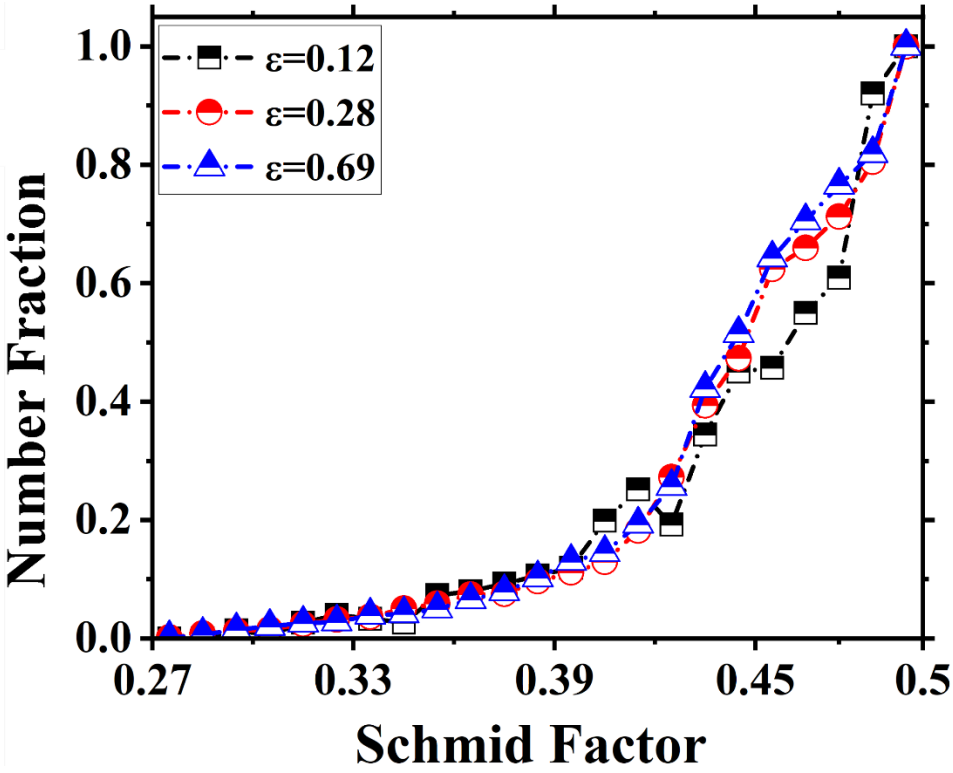

(d)

Figure 7: (a) Variation of the non-dimensional hardening, γ, and non-dimensional rate of strain-rate, α, as deduced from figure 1b, for the Al-6Mg alloy deformed at 573K. (b) High Resolution EBSD measurements at the MSB interface. These include Image Quality (IQ), Schmid factor and KAM maps – showing a percolating path of soft (high Schmid factor) grains and fragmentation thereof. (c) Network of grains of area smaller than 300 μm^2. Abutting small grains are connected by a red line. (d) Cumulative distribution of the Schmid factors of the fragmented grains identified in figure 7(c).

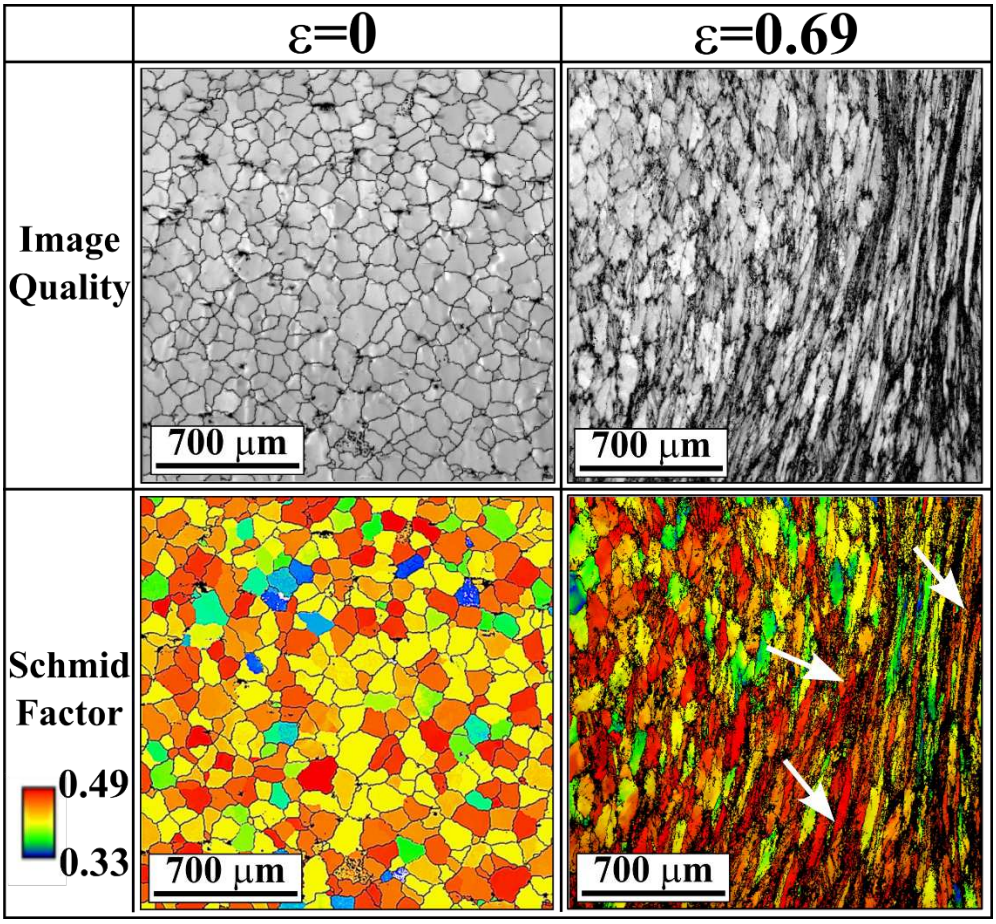
ε=0
ε=0.69
Image Quality
700 μm
700 μm
Schmid Factor
0.49
0.33
700 μm
700 μm

(a)

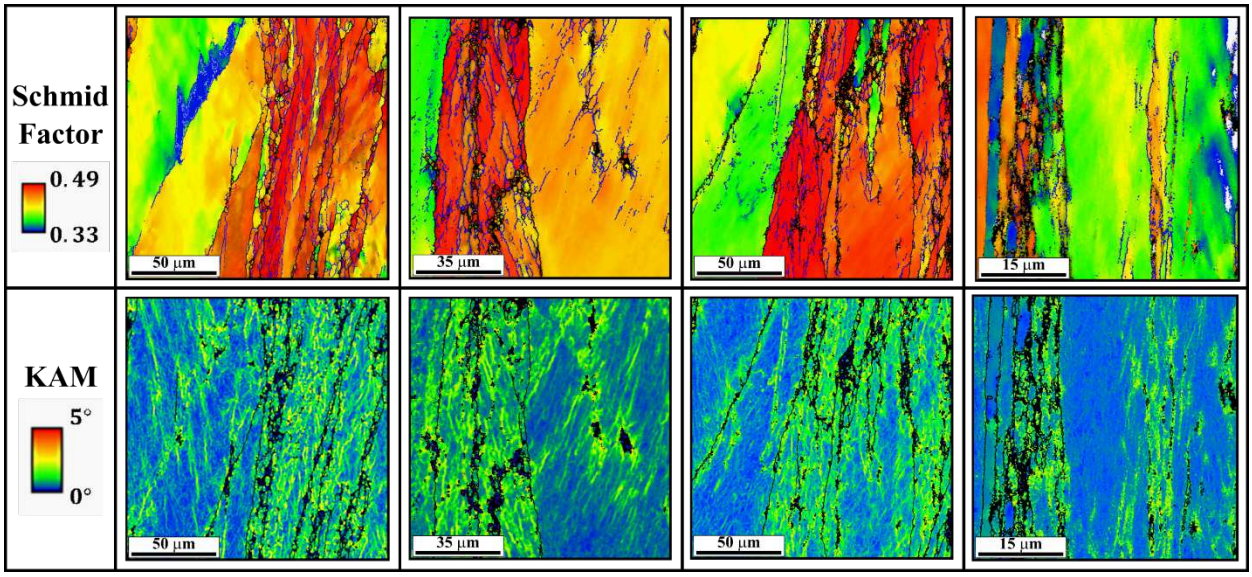
Schmid Factor
0.49
0.33
50 μm
35 μm
50 μm
15 μm
KAM
5°
0°
50 μm
35 μm
50 μm
15 μm

(b)

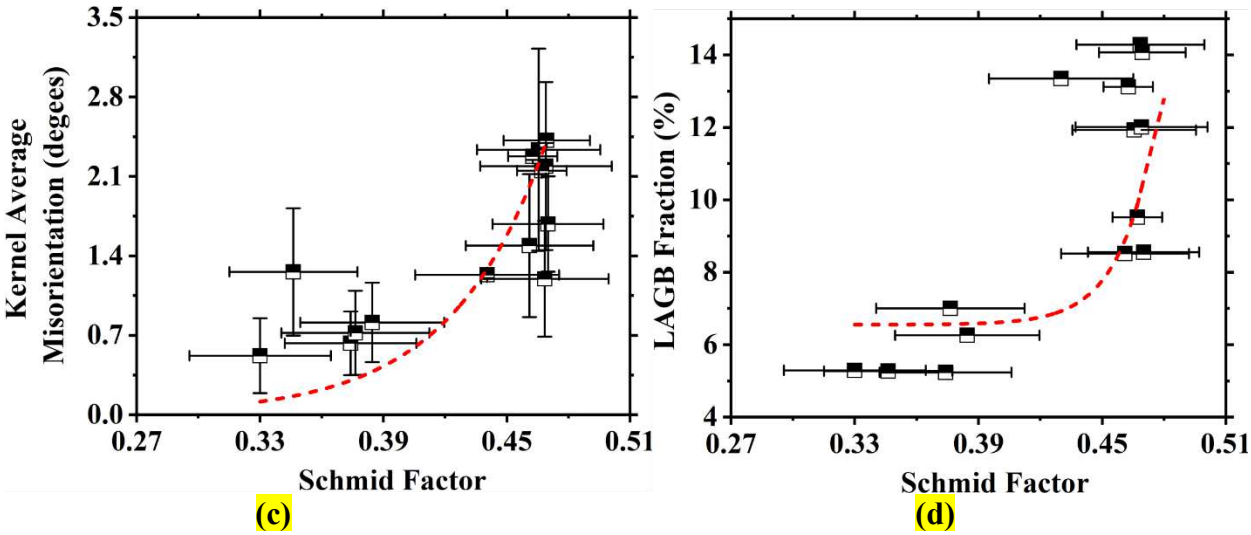

Figure 8: (a) EBSD measurements for specimens deformed up to ε=0 and ε=0.69. These include the Image Quality (IQ) and Schmid Factor maps. The arrows indicate the development of a percolating network of soft grains. (b) High Resolution EBSD (HR-EBSD) scans within the MSB for specimen deformed up to ε=0.69, represented using Schmid Factor and KAM maps. Boundaries highlighted in blue and black accommodate misorientations of 5°-15°, and $>15^{o}$, respectively. The variation of (c) the KAM and (d) the fraction of Low Angle Grain Boundary (LAGB) with Schmid factor within the MSB region of the deformed specimen.

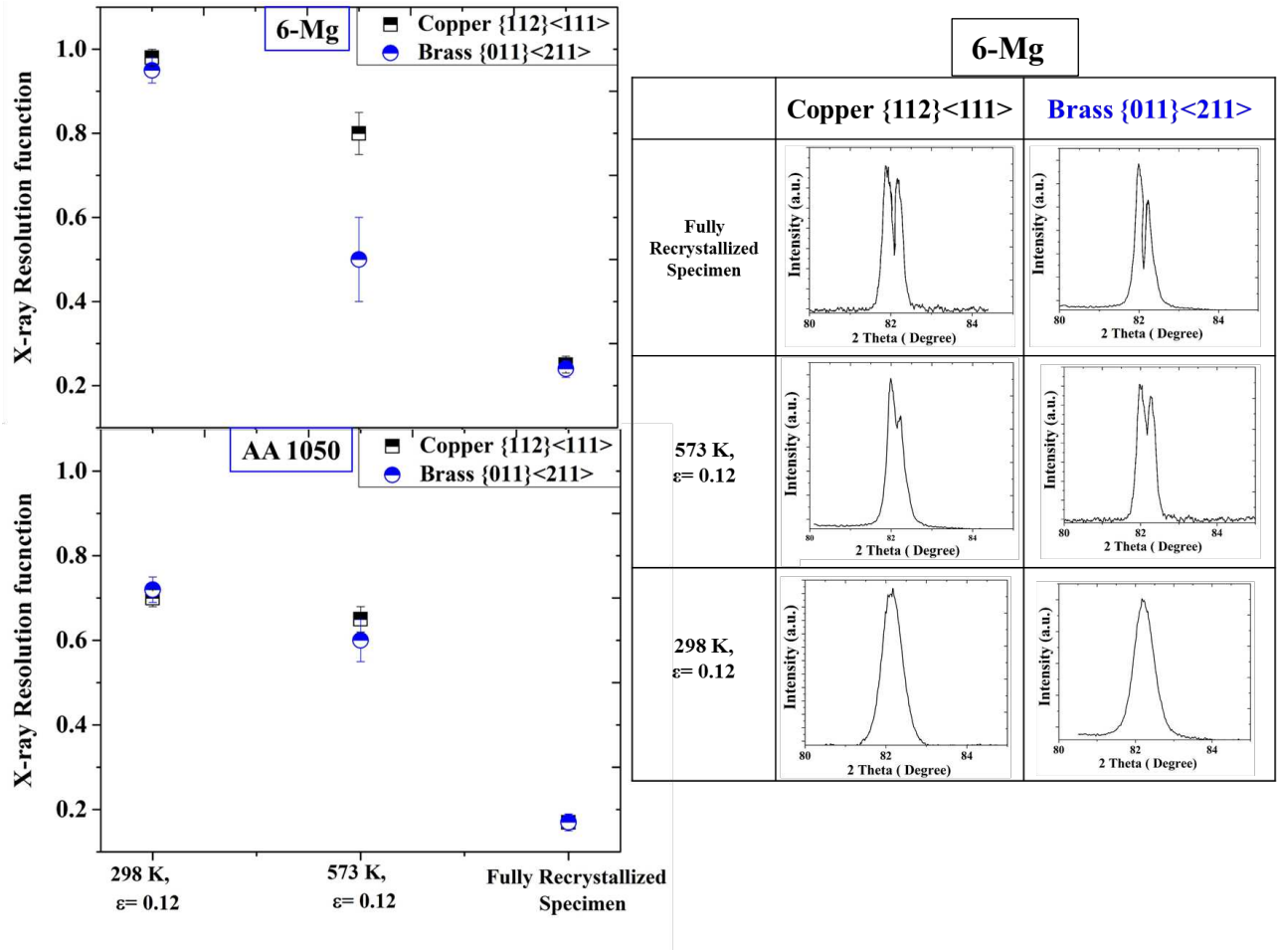
6-Mg
Copper {112}<111>
Brass {011}<211>
X-ray Resolution fucnction
1.0
0.8
0.6
0.4
0.2
AA 1050
298 K, ε= 0.12
573 K, ε= 0.12
Fully Recrystallized Specimen
Intensity (a.u.)
2 Theta (Degree)
80
82
84

(a)

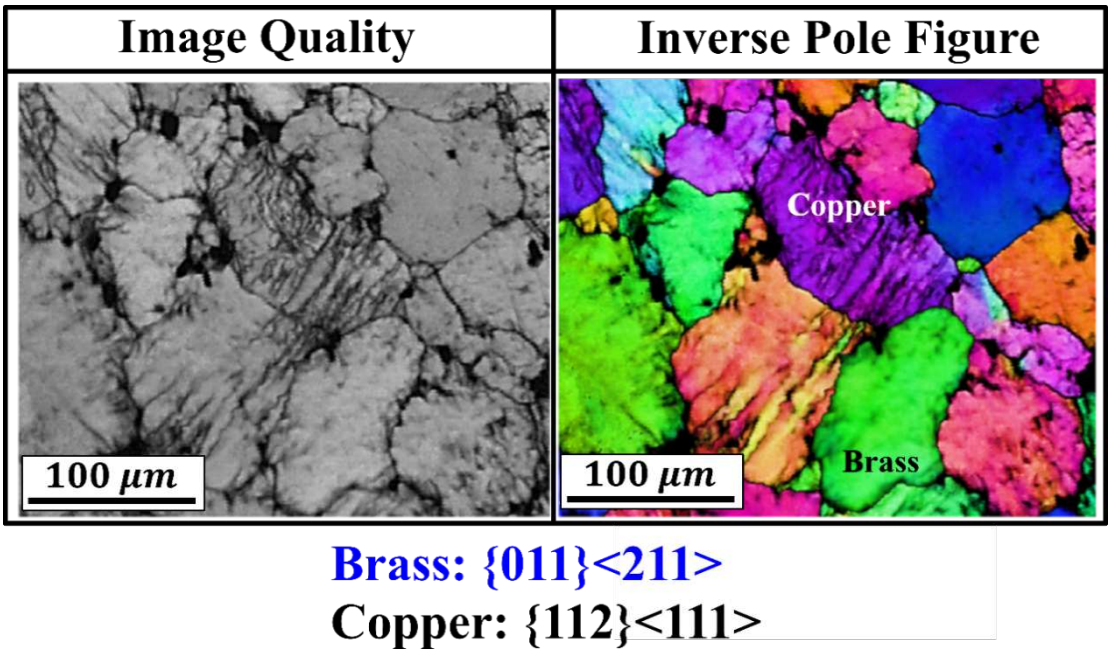
Image Quality
Inverse Pole Figure
100 μm
Copper
Brass
Brass: {011}<211>
Copper: {112}<111>

(b)

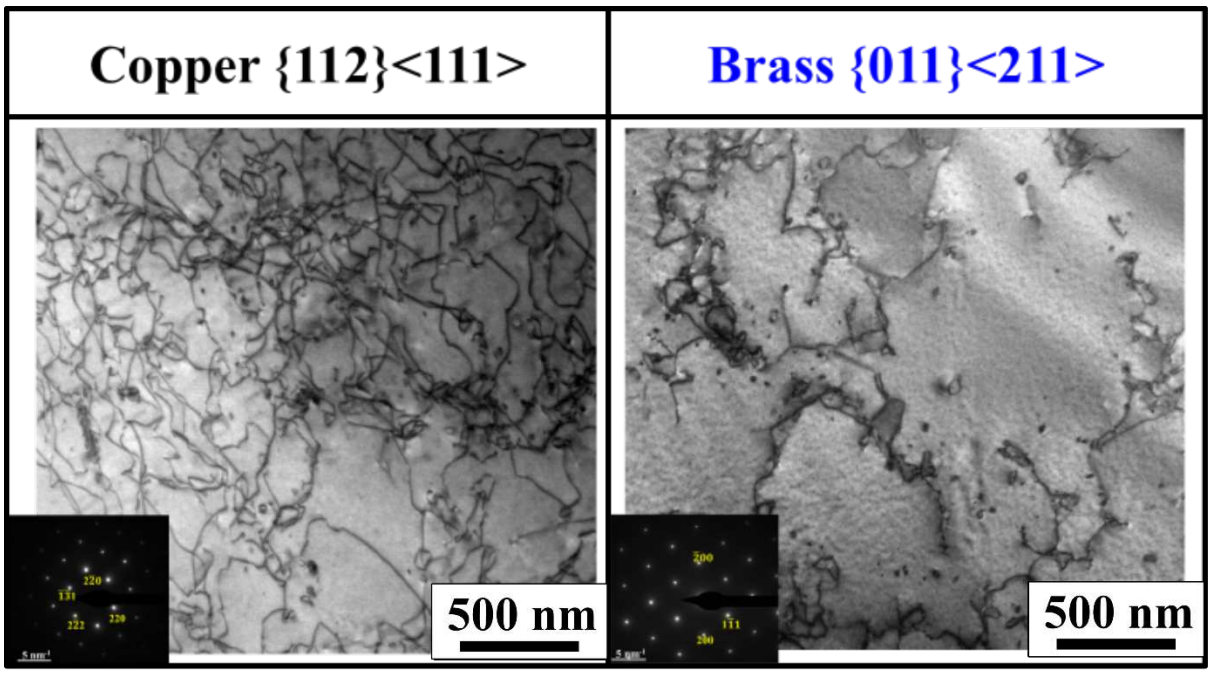

(c)

Figure 9: X-ray resolution function or XResF, see equation (8) [47,48] estimated for ideal Copper {112}<111> and Brass {011}<211> orientations using an area detector and appropriate goniometer rotations [37] in different specimens. Also included are examples of some of the XRD peak profiles (consisting of K□□ and K□□□) used to estimate XRF. (b) EBSD and (c) TEM showing substructures in Copper and Brass grains.

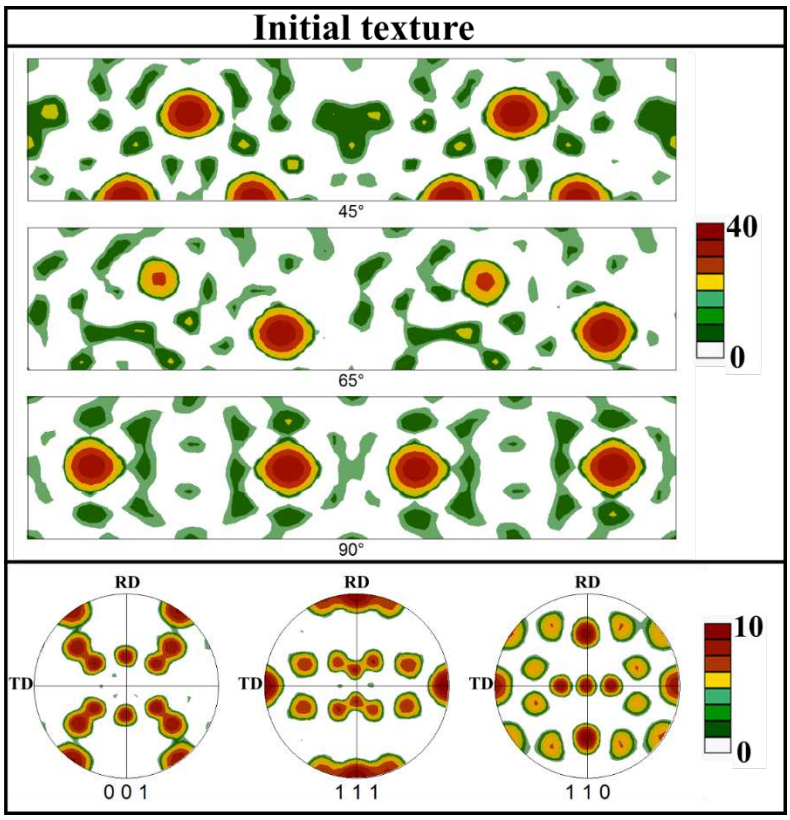
Initial texture
45°
65°
90°
40
0
RD
TD
0 0 1
1 1 1
1 1 0
10
0

(a)

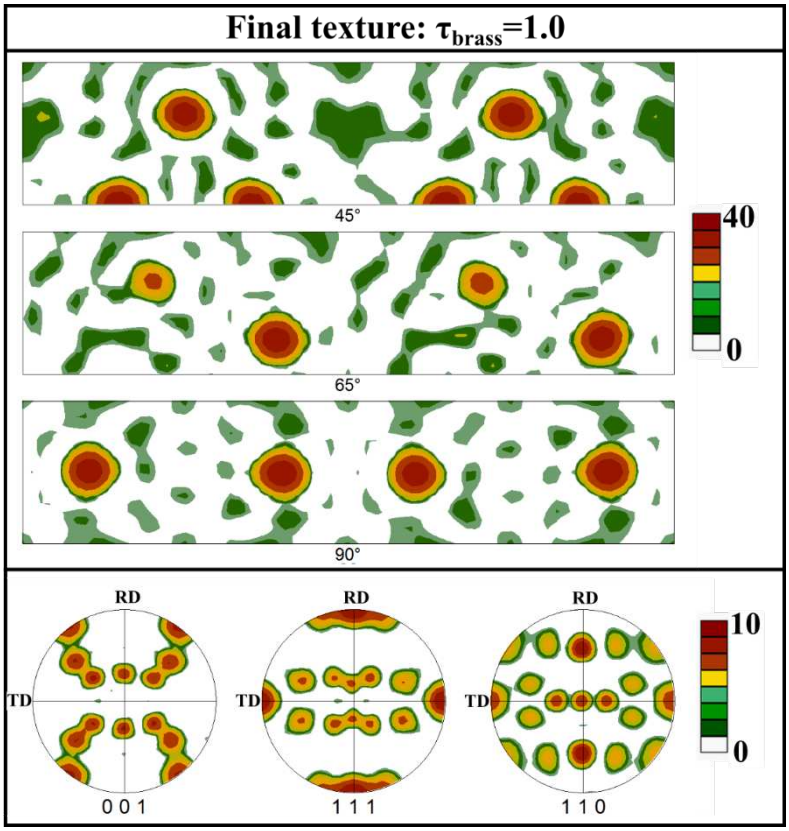
Final texture: τ_{brass}=1.0
45°
65°
90°
40
0
RD
TD
0 0 1
1 1 1
1 1 0
10
0

(b)

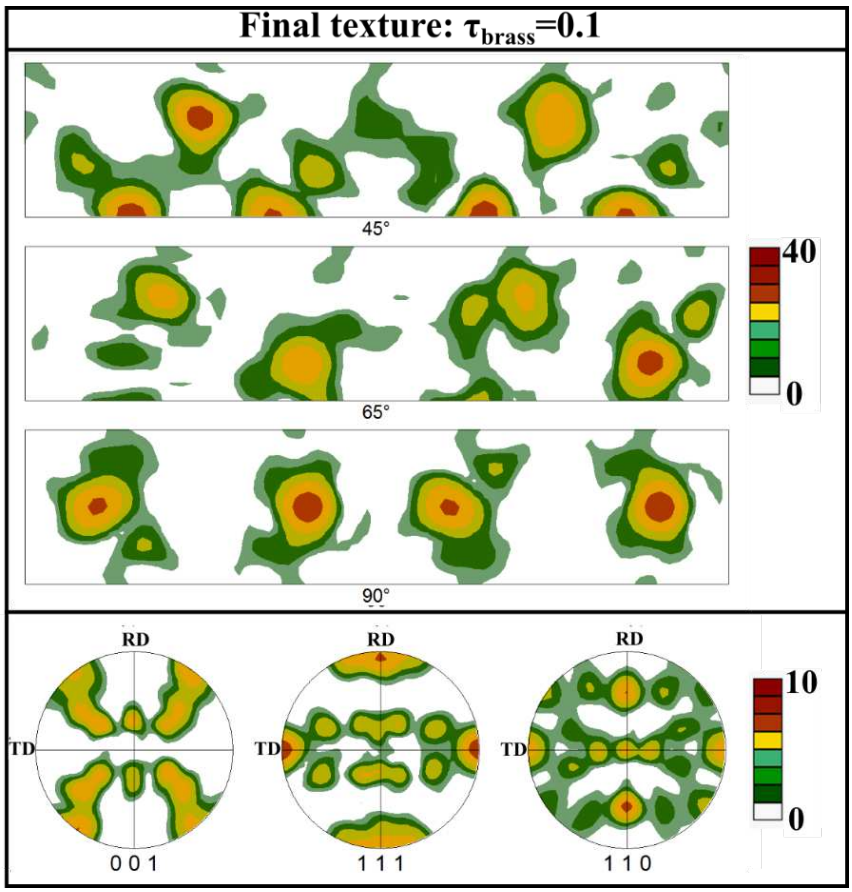
Final texture: τ_{brass}=0.1
45°
65°
90°
40
0
RD
TD
0 0 1
1 1 1
1 1 0
10
0

(c)

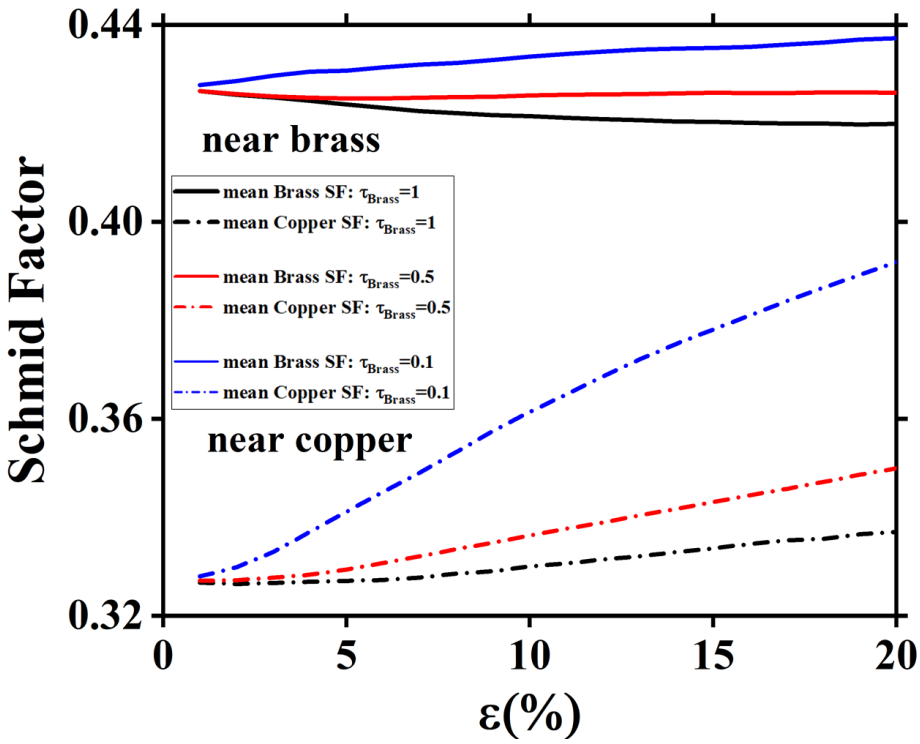
Schmid Factor
ε(%)
0.44
0.40
0.36
0.32
0
5
10
15
20
near brass
near copper
mean Brass SF: τ_{Brass}=1
mean Copper SF: τ_{Brass}=1
mean Brass SF: τ_{Brass}=0.5
mean Copper SF: τ_{Brass}=0.5
mean Brass SF: τ_{Brass}=0.1
mean Copper SF: τ_{Brass}=0.1

(d)

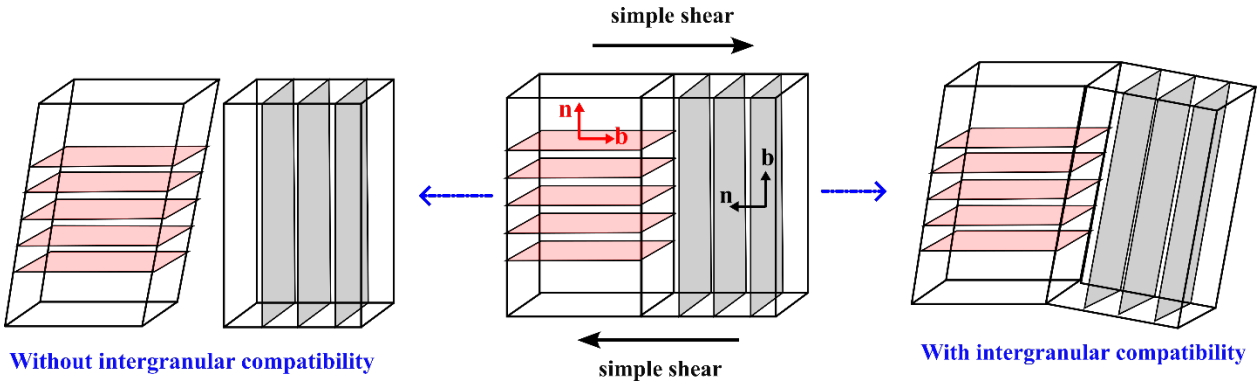

(e)

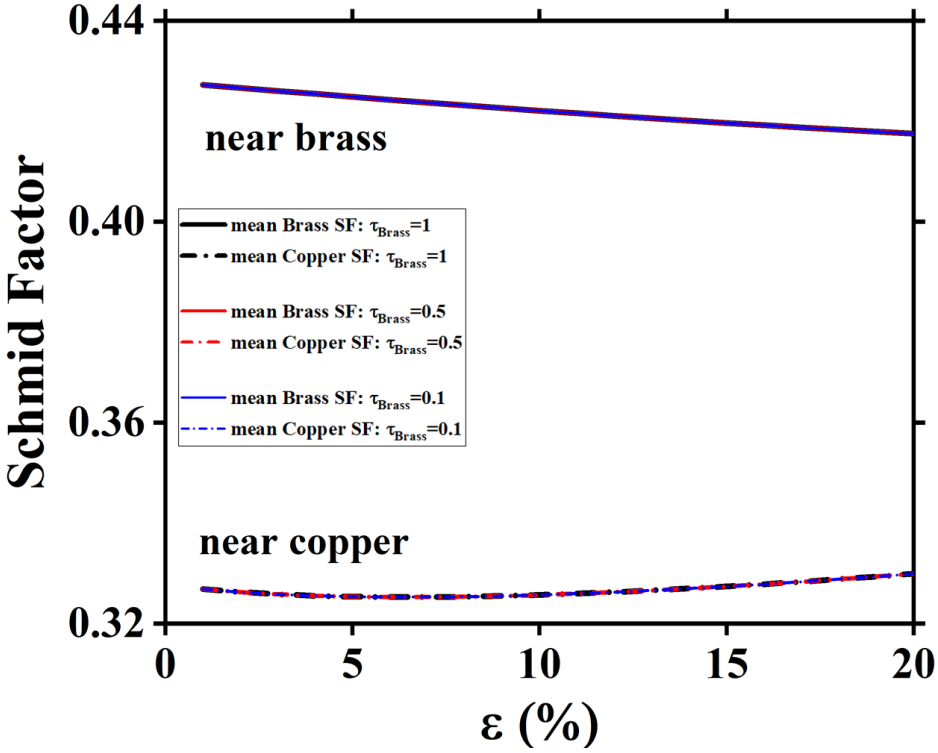

(f)

Figure 10: Schmid factor evolution with strain for an artificial polycrystal. (a) Initial texture of the polycrystal comprised of 50% near-brass and 50% near-copper oriented grains. Final texture after 20% rolling strain assuming that the CRSS of the near-copper grains is unity, and that of the brass grains is (b) 1.0, and (c) 0.1. (d) Mean Schmid factor evolution in the near-copper and near-brass grains corresponding to the CRSS of the near brass grains in {0.1, 0.5, 1.0}. (e) Schematic of the lattice rotation of a pair of neighbouring soft and hard grains, with and without enforcement of intergranular compatibility. (f) Mean Schmid factor evolution in the near-copper and near-brass grains predicted using the Taylor model.